Dipole-Trapped Atoms at High Optical Depth for Atom-Light Quantum Interfaces

Gianni C. Buser
Basel, July 2016

Abstract

Hybrid systems coupling ultracold atoms to different physical systems via light promise to have many quantum technological applications, including quantum information processing. In particular, hybrid systems with a mechanical component could be especially suitable for precision sensing, to read out the properties of a quantum mechanical system, and quantum signal transduction. In such systems the light-atom interface is an essential ingredient. The powerful and well understood control methods available for ultracold atoms form a solid foundation that more complex systems combining mechanical oscillators, quantum dots, or other quantum systems with these atoms build on. Theoretical models for advanced hybrid systems have developed and grown sophisticated in the past few years, but experimental implementations are still in earlier stages. Thoroughly optimising and characterising the light-atom interface component of such a hybrid system is critical for gaining understanding of and control over the hybrid system as a whole.

In this thesis I report on such an atom-light interface with $^{8}7$Rb atoms in a far-off-resonance dipole trap. The atoms trapped therein can either constitute half of an atom-membrane hybrid system, or they can be used as a quantum memory to store single photons emitted by semiconductor quantum dots. The elongated atom cloud has a full $1/e^2$ width of 74 µm and length around 26 mm. It consists of over 20 million atoms after 100 ms hold time, at a temperature of 54 µK, reaching a final value of 34 µK after a few seconds. Its on-axis resonant optical depth is higher than 1000, which translates directly into much higher light-atom coupling strengths than previously achieved. Further, I detail adapting an existing 1D optical lattice used for coupling atoms to a mechanical membrane oscillator to be loaded from this dipole trap, instead of from a MOT, and characterise the atomic ensembles both in the dipole trap and in the lattice. Finally, I conclude with preliminary atom-membrane interaction results and offer an outlook to the experiments this light-atom interface may be used for in the future.

Contents

Introduction

The interaction of light and matter is the broadest branch of optics. It informs our understanding of the universe on all scales, from the compositions of distant galaxies, to life on earth, to the behaviour of single atoms. It underlies processes on all energy scales, from pair production to the generation of the world's coldest matter, Bose-Einstein condensates. It is as relevant to technological applications as it is to probing the fundamentals of quantum mechanics.

Quantum information processing is likely to rely heavily on light-atom quantum interfaces, regardless of what quantum system or systems eventually triumph over the others to become the standard qubit. Qubits based on trapped ions [1, 2] or neutral atoms [3, 4] would require such interfaces directly for computation. Quantum communication, or more specifically entanglement distribution, based on photonic channels over long distances requires quantum repeaters and quantum memories. The coherence achievable in atomic states makes them exceptionally suitable for these tasks, so a quantum network would probably make use of atomic vapours or atomic ensembles, which were shown in [5] to efficiently implement a quantum repeater. These photonic channel based quantum network designs are sufficiently unique in their promise and feasibility that spin or charge based qubits would almost certainly use quantum signal transducers [6] to encode their quantum information onto light for transmission. Therefore light-atom quantum interfaces are a crucial building block in the endeavor of quantum information processing irrespective of the exact future technological advances in qubit implementations.

The goal of quantum information processing has guided modern experiments in light-atom interfaces due to its concrete requirements on scalability and control [7]. After it became possible to probe few or even single atoms, placed in cavities to enhance the interaction, the focus of light-atom interfaces lay mostly on these cavity experiments. More recently advances in laser technology have let atomic ensembles grow in favour. There the strong, cavity enhanced interaction of one atom is matched by the contributions of many atoms interacting less strongly. Varied interfacing mechanisms including electromagnetically induced transparancy, Faraday interactions, Raman interactions, and others have established themselves as viable [8], and methods and protocols for working with the collective, continuous variables of an atomic ensemble in terms of information processing have been developed [9].

Meanwhile, and independently of the successes achieved in light-atom interfaces, the quality of and control over other quantum systems advanced. In this context the

concept of a hybrid system that attempts to combine different systems emerges naturally. Hybrid systems come in different flavours. They may strive to take advantage of each subsystem's superior attributes to achieve an overarching goal, or they may aim to transfer the advanced control schemes available for one of their constituents to the other. An example of the former, a best-of-both-worlds type hybrid system, is an atomic quantum memory for single photons from a GaAs quantum dot [10]. In [11] bright, robust, and fast quantum dots with close-to-ideal properties were demonstrated at 780 nm. These excellent light sources are then combined with atomic memories, which have been shown to provide long storage times and high efficiencies, for example in [12].

An implementation of the latter is found in the field of atom-optomechanics, where macroscopic mechanical oscillators are coupled to atoms via light [13]. This hybrid system can be implemented, for instance, by trapping an atomic ensemble in an optical lattice retroreflected on a micromechanical membrane, coupling the motion of the atoms in the lattice to the vibrations of the membrane [14, 15]. Using this scheme it is possible to sympathetically cool the membrane from room temperature to 650 mK [16]. With continued progress this type of system can hope to cool lower frequency vibrational modes of larger membranes than previously demonstrated [17] to their phononic ground state, where quantum mechanical operations such as state swaps could be performed.

At first glance it is perhaps surprising that the figure of merit for the atom-membrane coupling strength and for the quantum memory efficiency is the optical depth of the atom cloud [8, 18, 19]. The connection becomes clear when considering that in order for atoms to interact with light they must absorb or scatter it. Its importance has lead some authors to recast the methods developed in the 1990s to load traps efficiently and compress atom clouds to increase phase space density in pursuit of Bose-Einstein condensation as methods to optimise optical depth [20]. This renewed focus on loading traps and cooling atom clouds promises to pay off with access to the strong coupling regime in hybrid systems, where a lot of interesting physics awaits.

Against this background, ultracold atoms in a far-off-resonance optical dipole trap present themselves as an excellent candidate. Loading this type of trap efficiently has been studied in detail [21]. Lacking strong confinement along the optical axis for a not too strongly focused beam, the desired geometry of a highly prolate atom cloud is automatical realised after a short time, even when loading from a spherical MOT. In the far detuned case the trap potential can be made independent of the hyperfine state, and photon scattering events are so rare that the lifetime of the atoms in the trap is determined by background gas collisions. This means typical lifetimes range from 1 s to 100 s, depending on the quality of the vaccuum. These features allow both low-loss manipulation of the atomic state and long, adiabatic ramping without concern for atoms being heated away [22]. Additionally, consisting of a single beam, these traps are comparatively simple to set up and maintain.

This thesis discusses the design, setup, and characterisation of a far-off-resonance optical dipole trap for ultracold ^{87}Rb atoms for use in hybrid systems, with the specific goal of achieving high optical depth. I present the context of the rest of the experimental setup, and give a brief theoretical overview of dipole traps in chapter 1. I place

most theoretical calculations directly preceding their experimental evaluations to facilitate comparison. Chapter 2 contains the full characterisation of the dipole trap and the trapped atomic ensemble. Then, in chapter 3, I discuss loading a 1D optical lattice from the dipole trap and I characterise this lattice. I find that I can transfer many of the advantageous attributes of the atom cloud from the dipole trap to the lattice, but that some technical details still need to be addressed to ensure that the process is adiabatic. In chapter 4 I conclude by presenting the results of a first attempt, with the new setup, at coupling the atoms to a mechanical membrane, and I outline a possible future path of our hybrid systems experiments.

Chapter 1

Dipole Trap Design

The optical dipole trap that is the main topic of this work is an upgrade to a functioning experimental setup. The pre-existing cold atom apparatus is described in great detail in [23], and interim improvements, esspecially to our imaging system, are detailed in [18]. This chapter provides a minimal overview of these systems adapted from these sources, for the purpose of context, and omitting all details not directly relevant to the additions. Next, the basic theory of optical dipole trapping of alkali atoms is reviewed, leading to a realistic model of the trapping potential. Finally, the atom cloud that can be confined in this trap is studied theoretically, and some geometrical considerations are discussed.

1.1 Overview of the Pre-existing Setup

1.1.1 The Cold Atom Apparatus

Our cold atom apparatus implements many of the standard techniques for preparing ultracold atomic ensembles of ^{87}Rb atoms [24]. The heart of the system is a small, octagonal, glass cell under ultra high vacuum, with a pressure on the order of 10^{-9} mbar. This chamber, depicted in figure 1.1, sits in the middle of a raised breadboard above the optical table. Attached to the cell are a pair of coils near anti-Helmholtz configuration which create the magnetic field gradients necessary for a three-dimensional magneto-optical trap (3D-MOT). Further away a cage of three pairs of much larger Helmholtz coils compensate unwanted external magnetic fields and set the quantisation axis for imaging and optical pumping.

On the optical table below light is split into six counterpropagating 3D-MOT beams before they are directed up to the glass cell. Figure 1.2[1] shows the optical axes in the plane of the breadboard level. The 3D-MOT is loaded from a two-dimensional MOT (2D-MOT), which captures atoms from the ambient vapour of a natural rubidium source, and transfers them to the 3D-MOT via an atom beam. Orthogonal to the

[1] This figure, and other figures showing optical elements in a schematic style, were all drawn with the aid of ComponentLibrary by Alexander Franzen [25].

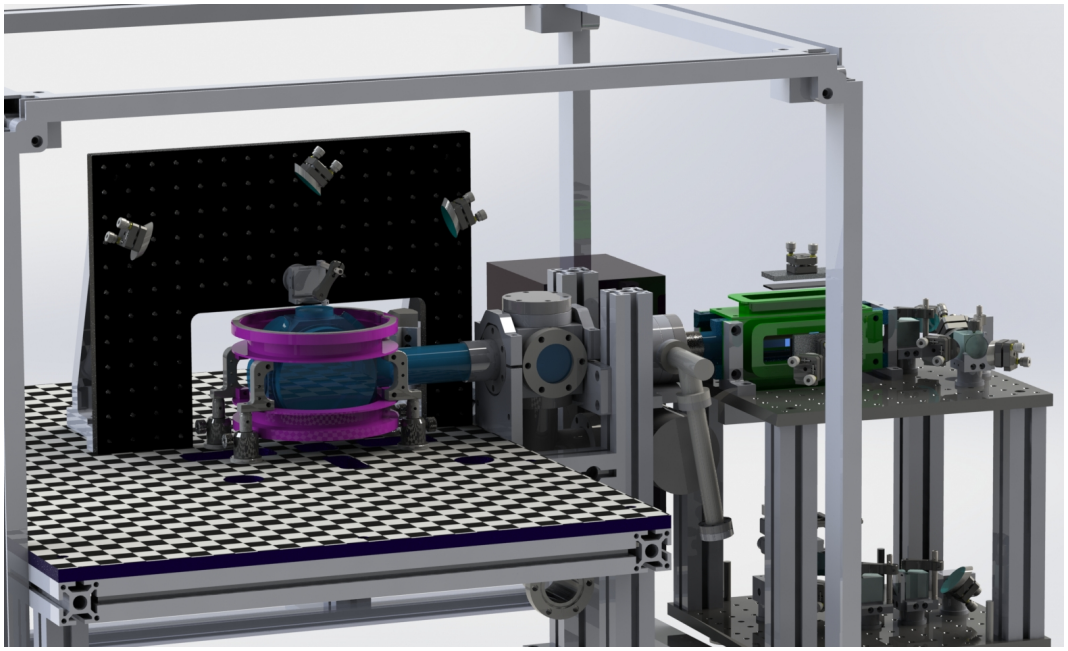

Figure 1.1: An uncluttered rendering of the permanent setup of our cold atom machine. The main vacuum chamber and its connection to the pumps and the 2D-MOT is shown in turquoise. The 2D-MOT chamber is coloured green. Its light is prepared on a kind of breadboard annex to allow the atom beam to enter the main vacuum chamber at a small angle. The coils for producing the field gradients for the 3D-MOT are shown in pink. The compensation coils are embedded in the large cage surrounding the setup. The holes in the breadboard, drawn with a chequerboard pattern for contrast, are for bringing up the light for the 3D-MOT from the optical table below. See figure 1.2 for an overview of all the optical axes.

main axis light is directed through the atom cloud onto a CDD camera,[2] which grants a side-view of the atom clouds trapped in the dipole trap or the optical lattice.

Details on the operation of this MOT for the purpose of loading the optical dipole trap may be found in section 2.1.2.

1.1.2 Absorption Imaging

When appropriately calibrated, absorption imaging [26, 27] provides information about the geometry, atom number, density, and temperature of atom clouds. Circularly polarised light is sent through the atom cloud, where it scatters on the $|F = 2, m_F = 2\rangle \leftrightarrow |F' = 3, m'_F = 3\rangle$ cycling transition of the ^{87}Rb D_2 line, which is defined by a small magnetic field (0.1 mT) along the imaging axis, and an image is taken of the light that remains. Just before the image is taken, the $F = 1 \rightarrow F = 2$ repumping beams are switched on and a short $F = 2 \rightarrow F = 2$, σ^+ polarised pumping pulse is applied to

[2] Manta G-145B MOD RCG by Allied Vision Technologies GmbH

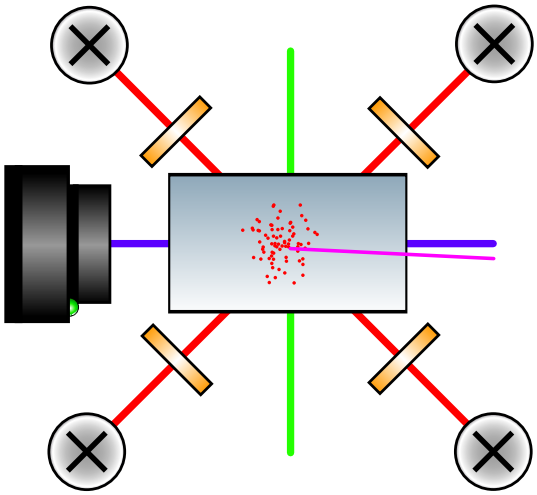

Figure 1.2: In the plane of the breadboard four optical axes cross in the vacuum cell. The optical dipole trap and the one-dimensional optical lattice run along the main optical axis, shown in green. Their optics are omitted here as more detailed drawings are shown in sections 2.1 for the dipole trap and 3.2 for the optical lattice. The black crosses represent the upper periscope mirrors, directing four of the six counterpropagating MOT beams, drawn in red, through quarter-wave plates and into the vacuum cell. The third pair of 3D-MOT beams run vertically through the chamber, which would be orthogonal to the page here. The blue line represents the side-view imaging axis. Finally, the pink line represents the atom beam from the 2D-MOT.

prepare the atoms in the appropriate hyperfine state for imaging.

Additionally, it is necessary to take a reference image without atoms. Usually, the goal is to see the atoms under ballistic expansion, so, typically, all light beams and fields are abruptly switched off before imaging. If this is not the case, then they are instead switched off after taking the image of the atoms. Either way, the atoms are allowed to fall away and a reference image is taken soon after the atoms have completely left the field-of-view. For greater accuracy in the presence of stray room light the imaging beam can be turned off to take a dark image. Our cameras are shielded from most stray light by the lens tubes that house their imaging lenses. Therefore, our experimental sequences do not take new dark images for every run by default.

With the intensities in these three images we can now define the measured optical depth as

$$\mathrm{OD}(x,y) \coloneqq -\ln\left(\frac{I_{\mathrm{atoms}}(x,y) - I_{\mathrm{dark}}(x,y)}{I_{\mathrm{ref}}(x,y) - I_{\mathrm{dark}}(x,y)}\right). \tag{1.1}$$

In the limit of low saturation the optical depth can be related to atomic density via the Beer-Lambert law [27]

$$\mathrm{OD}(x,y) = \sigma \int n(x,y,z)\,dz =: \sigma\tilde{n}(x,y), \tag{1.2}$$

where σ is the scattering cross section,

$$\sigma = \frac{\sigma_0}{1 + \left(\frac{2\Delta}{\Gamma}\right)^2}. \tag{1.3}$$

Here $\sigma_0 = \frac{3\lambda^2}{2\pi}$ is the resonant scattering cross section for σ^+ light driving the cycling transition [28]. If $\Delta = 0$, then the optical depth is called the resonant optical depth, OD_{res}. For an OD measured off-resonantly the equivalent resonant OD is simply $\mathrm{OD}_{res} = \left(1 + (2\Delta/\Gamma)^2\right) \mathrm{OD}$.

Equation 1.3 warrants some further comments. Absorption imaging is quantitatively reliable for optical depths, in the sense of equation 1.1, up to 3 or 4 [27], as cameras have a finite dynamic range. For this reason it may be necessary to image dense clouds off-resonantly. The term $2\Delta/\Gamma$ explains what happens when the imaging light is detuned from the imaging transition. That is, less scattering occurs and lower ODs are measured. Technically, there would be a third term in the denominator, I/I_{sat}, describing a saturation effect. The saturation intensity is an intrinsic property of the transition. Its value is $I_{sat} = 1.67\,\mathrm{mW\,cm^{-2}}$ for σ^+ light driving the cycling transition [28]. To reduce our sensitivity to uncertainties in the calibration of the imaging system [18] we use a low imaging intensity ($0.2\,I_{sat}$), so that this term can be neglected. It would, however, also be possible to image in the regime where the imaging intensity is much greater than the saturation intensity [27].

1.2 Theory of Dipole Trapping

When light is incident on atoms it shifts the energy of the atomic states via the AC Stark shift. For this reason it is possible to create a potential well for atoms simply by focusing a laser beam onto them, and thus to trap them. The approaches to calculating the dipole potential experienced by atoms in the presence of laser light vary greatly in scope and depth. It is possible to do so fully classically, as is often done in textbooks on electrodynamics, as well as in some reviews [22, 29]. Alternatively, or subsequently, the semi-classical approach of a two-level atom in a classical radiation field is typically taken [30, 31]. Unfortunately, neither of these approaches correctly treat spontaneous emission. The classical damping rate given by Larmor's formula is only good for approximations, unless corrected by the empirical oscillator strengths [32], and quantised atoms in a classical field do not decay from their excited states in the absence of light at all [33]. For this reason, the result of a fully quantised calculation originally by Wigner and Weisskopf, namely

$$\Gamma = \frac{\omega_0^3}{3\pi\epsilon_0\hbar c^3} \left|\langle e|\mu|g\rangle\right|^2, \tag{1.4}$$

is often introduced in an ad-hoc manner with little context. This result is also subject to some approximations and can be further improved with higher order terms [34].

Another point where descriptions diverge is in addressing the fact that atoms have not two but many energy levels. First, the selection rules for these transitions coming

from the conservation of orbital angular momentum can be used to find all allowed transitions between states [24]. Then the determining factor becomes whether the frequency of the laser, ω, is near the resonance frequency, ω_{ij}, of the transition between two levels of the atom i and j [22]. (Note that when only a single transition frequency is involved ω_{ij} is called ω_0 to continue distinguishing it from the laser frequency ω.) That is, the most significant transitions are those for which the detuning of the laser $\Delta_{ij} \coloneqq \omega - \omega_{ij}$ is smallest, possibly allowing a reduction of the atom to a two-level system. For example, if the detuning from the D_2 line is much smaller than the detuning from the D_1 line, then the D_1 line can be neglected. This is not to imply that the detuning is necessarily absolutely small with respect to any transitions to allow approximations, only relatively smaller. Additionally, for a sufficiently large detuning from a specific transition, the hyperfine structure of the involved levels will not be resolved and can usually be neglected, in the sense that the many levels are treated as one. Independently of which transition is considered, should the detuning additionally be small in comparison to the sum of the laser and transition frequencies, i.e. $\Delta_{ij} \ll \omega + \omega_{ij}$, then the rotating wave approximation (RWA) may be made to further omit the terms proportional to $e^{\pm(\omega+\omega_{ij})}$ from the Hamiltonian [29]. On the other end of the spectrum, every day highly precise calculations using relativistic all-order methods are used to create extensive theoretical tables of atomic properties (e.g. in [35]), which are collected and meticulously checked against measurements by the precision spectroscopy community [36].

Bearing all that in mind, as well as the plethora of sources that cover the optical dipole interaction, including almost all quantum optics textbooks, this chapter states the dipole potential relevant for our purposes and motivates its form, without claiming to give a thorough and comprehensive derivation. Instead some attention is later paid to the geometric properties of the atom cloud confined in this potential.

1.2.1 The Dipole Potential

The dipole interaction Hamiltonian is $\mathcal{H}_1 = -\hat{\boldsymbol{\mu}}\mathbf{E}$, where the nature of $\mathbf{E}$ is determined by the model. (This is, within the semi-classical model it is a classical field, and within the quantum model it is the corresponding operator.) We begin with the general result of second-order perturbation theory for the shift for an energy level i, where j indexes over all other possible states

$$\Delta E_i = \sum_{j \neq i} \frac{|\langle j|\mathcal{H}_1|i\rangle|^2}{\mathcal{E}_i - \mathcal{E}_j}, \tag{1.5}$$

where $\hat{\boldsymbol{\mu}} = -e\hat{\mathbf{r}}$, $-e$ is the elementary charge, and $\hat{\mathbf{r}}$ is the electron position operator. To get a first impression we evaluate this equation [22, 30] with the RWA and assuming a two-level atom with the states $|g\rangle$ and $|e\rangle$. In the denominator, taking the dressed state view, we compare the internal energy of a ground state atom (0) plus the energy of n photons ($n\hbar\omega$), with the energy of an excited state atom ($\hbar\omega_{eg}$) plus the energy of $n-1$ photons. This yields $n\hbar\omega - (n-1)\hbar\omega - \hbar\omega_{eg} = \hbar\Delta_{eg}$. With the aid of equation

1.4 we now find the ground state energy shift to be

$$\Delta E_g = \frac{|\langle e|\mu|g\rangle|^2}{\hbar\Delta_{eg}}|E|^2 = \frac{\hbar 3\pi c^2}{\hbar 2\omega_{eg}^3}\frac{\Gamma_{eg}}{\Delta_{eg}}2\epsilon_0 c|E|^2 = \frac{3\pi c^2}{2\omega_{eg}^3}\frac{\Gamma_{eg}}{\Delta_{eg}}I, \tag{1.6}$$

where $I = 2\epsilon_0 c|E|^2$ is the intensity of the incident laser light. If the atoms reside in the ground state most of the time, then this expression describes the potential determining their motion.

To get more concrete, we consider the case of ^{87}Rb confined in a single beam dipole trap at 1064 nm. The rubidium D-lines are at 795 nm (D_1) and 780 nm (D_2). The laser detuning is so large that both of these transitions need to be considered. As long as the laser detuning is much larger than the excited state hyperfine structure, the additional transition can be taken into account with equation 1.5, specifically for the ground state $|F, m_F\rangle$ the potential is [22]

$$U_{\text{dip}} = \frac{\pi c^2}{2\omega_{eg}^3}\left(\Gamma_{D_2}\frac{2+\mathcal{P}g_F m_F}{\Delta_{D_2}} + \Gamma_{D_1}\frac{1-\mathcal{P}g_F m_F}{\Delta_{D_1}}\right)I \tag{1.7}$$

where $\mathcal{P} = [0, \pm 1]$ for $[\pi, \sigma^{\pm}]$ polarised light.

Furthermore, for both of these transitions $\omega - \omega_{ij}$ is a little less than one sixth of $\omega + \omega_{ij}$, hardly much smaller. Thus, the RWA also introduces a significant error. the RWA omits terms proportional to $e^{\pm(\omega+\omega_{ij})}$. In a fully quantised model it is difficult to treat these counter-rotating terms simultaneously with the rest, but semi-classically it is quite simple to derive that for a single transition [22]

$$U_{\text{dip}} = \frac{3\pi c^2}{2\omega_0^3}\left(\frac{\Gamma}{\omega-\omega_0} - \frac{\Gamma}{\omega+\omega_0}\right)I. \tag{1.8}$$

To bridge the gap between equations 1.7 and 1.8 we can insert the information that our laser is linearly polarised to find the relative weights of the D_1 and D_2 lines in equation 1.7, then apply these to equation 1.8 as it would be written for the D_1 and D_2 lines separately, forming a weighted sum:

$$U_{\text{dip}} = \pi c^2\left(\frac{\Gamma_{D_2}}{\omega_{D_2}^3}\left(\frac{1}{\omega-\omega_{D_2}} - \frac{1}{\omega+\omega_{D_2}}\right) + \frac{1}{2}\frac{\Gamma_{D_1}}{\omega_{D_1}^3}\left(\frac{1}{\omega-\omega_{D_1}} - \frac{1}{\omega+\omega_{D_1}}\right)\right)I. \tag{1.9}$$

This is the final and most accurate form of the dipole potential for our far off resonance dipole trap, although in the interest of brevity the last step in the dervation was somewhat sloppy. Usually when this equation is derived [37, 38] a fully classical calculation is performed, whereupon the correct weighting of of each term is, by definition, that of the transition's oscillator strength [32]. To arrive at the above form this classical oscillator strength is converted into the quantum mechanical quantities Γ and a Clebsh-Gordon coefficient [28]. Also note that in all these equations the fact that the potential is attractive and actually confines atoms as opposed to repelling them is hidden away in the sign of the detuning, which is negative when the laser is to the red of the transition.

1.2.2 Trap Design Considerations

The question now arises how the potential given in equation 1.9 can be set experimentally to trap atoms. In some experiments the exact wavelength of the trapping laser is important. For instance, in optical clocks [39] and in precision measurements [40] the measurement accuracy and stability can be dramatically improved by using the magic wavelength. At this wavelength the ground and excited states of the optical transition of interest experience the same light shift from the trapping light. Excluding those cases, for traps near resonance the atom-laser detuning Δ, or more specifically the laser frequency ω can be changed on a meaningful scale with acousto-optical modulators (AOMs). In this scenario the detuning can be used to define the potential, as well as what physical processes will be significant for the trapped atoms. In our case the detuning is so large that creating a significant change would require tens, or better hundreds of nanometres tuning range, so this parameter is out. Instead our experimental access comes from the beam's intensity profile. For a focused Gaussian beam propagating along z that is

$$I(r,z) = \frac{2P}{\pi w^2(z)} e^{-2\frac{r^2}{w^2(z)}} \tag{1.10}$$

where P is the power and $w(z)$ is the width of the beam given by

$$w(z) = w_0 \sqrt{1 + \frac{z^2}{z_R^2}}, \tag{1.11}$$

where w_0 is the waist, i.e. the $1/e^2$ radius at the focus ($z = 0$), and $z_R = \frac{\pi w_0^2}{\lambda}$ is the Rayleigh range. Effectively the adjustable parameters of the trap are therefore just P and w_0, as Δ is fixed by the choice of the laser and the polarisation is chosen to be linear so that the trapping potential is independent of the atom's m_F state. The theoretical details and calculations to that end fill the rest of this chapter, wherein I have benefitted from the experiences of those who have set up similar dipole traps before [37].

As I dicussed to motivate this endeavour, the figure of merit for judging the quality of diverse atom-light quantum interfaces is the optical depth [8]. Depending on the application, inefficiencies are typically proportional to $1/\mathrm{OD}$ or $1/\sqrt{\mathrm{OD}}$. As we found in equation 1.2, a higher axially integrated density results in a higher OD. Thus, ideally, our trap will be narrow, elongated, and as full of atoms as possible. In section 2.3 the interplay of the OD with atomic and trap parameters is examined further, but the optimisation problem is difficult to tackle systematically because narrower traps are less elongated and load fewer atoms.

With that in mind, the considerations for choosing the waist of the dipole trap beam were mainly qualitative and practical. As we will discuss shortly, the size of the atom cloud confined in a single beam dipole trap is significantly smaller than the beam itself. If an experiment or measurement calls for mode matching a beam to the trapped atomic sample, implying that the beam and the atomic sample have similarly

sized waists, then a narrow waist would necessitate fine alignment and great pointing stability. In our setup, when performing a measurement series with hundreds of shots after having newly aligned optics the position of the atom cloud can be seen to drift, typically on the order of $1\,\mu\mathrm{m\,h}^{-1}$, as various screws relax in their mounts. For this reason atomic samples with waists between 10 µm and 20 µm are already much easier to work with than ones with waists smaller than 10 µm. Conversely, the beam waist must not be too broad so that the trap is sufficiently deep to be loaded. With a maximum available power of 21 W the trapping beam must be at least sufficiently focused to produce a potential that can confine atoms at the minimum temperature in the MOT of 200 µK [18].

After a quick test of the available precision lenses we settle on the most strongly focusing one, which results in $w_0 \approx 90\,\mu\mathrm{m}$. The issue of an exact determination of the beam waist will come up repeatedly throughout this thesis. It was measured directly via beam profiling on a mock setup to be 92 µm, but later measurements of the trap frequency and trap depth require it to be slightly different to be self-consistent. In all following calculations I've decided to use the beam waist determined self-consistently from the trap frequency measurement described in section 2.4.1, which is $w_0 = 85\,\mu\mathrm{m}$.

With this beam waist and the 21 W of available power equation 1.9 yields a maximal trap depth, $T_d = U_{\mathrm{dip}}(r = 0, z = 0)/k_B$, of $-282\,\mu\mathrm{K}$. (Note that some authors prefer to eliminate the minus sign when expressing potentials in units of temperature or frequency. I have refrained from this despite the somewhat unusual appearance so that the attractive nature of the potential is not obscured.) We can be optimistic that at this trap depth loading will take place during the cold MOT stages, and find no motivation to reduce the trap depth right away. Thus, unless explicitly stated otherwise, all further numerical calculations concerning the dipole trap use $P = 21\,\mathrm{W}$ and $w_0 = 85\,\mu\mathrm{m}$. The first of these is shown in figure 1.3, where the spacial profile of the dipole potential is plotted.

To illustrate the point about mode matching a probe beam to the atomic sample we now take these dipole trap parameters as given and discuss the optimisation of a simple experimental situation. Consider the case of a single pass pulsed probe beam interacting with the atoms. To optimise the signal to noise ratio of whatever the atoms are to impart onto the light field (presumably a phase, polarisation, or intensity shift) this probe beam would need to be mode matched to the atomic sample, not to the trapping beam [41]. A simple picture gives the correct intuition. If the probe beam is larger than the atom cloud the light that passes the atoms without interacting increases the noise. On the other hand, a probe beam smaller than the atom cloud will suffer a reduction in signal from not interacting with all the atoms. A detailed model including diffraction effects may be found in [41]. In the specific case of the chosen dipole trap parameters and an atom temperature of 33 µK the atom cloud would have a waist of 29.1 µm and the optimal probe beam would have a waist of 27.7 µm, where both values refer to the radius at the $1/e^2$ level. The alignment of beams this size would certainly be stable enough for experiments although possibly requiring regular adjustments.

This example does not quite represent the current experimental situation. Nevertheless, it is a common case (compare for instance [42]), and allowing for it now

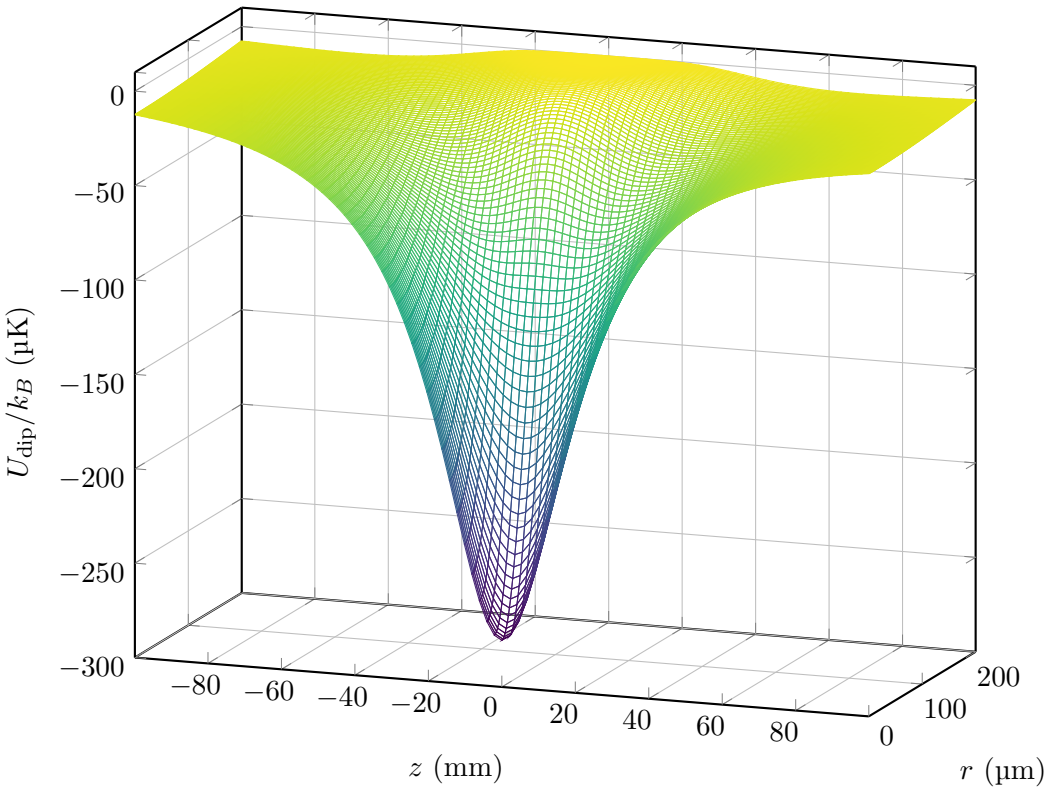

Figure 1.3: The potential of the dipole trap. Note the scale of the z-axis - the deepest region of the trap (full width at the 10 % level) extends over almost 15 mm.

potentially goes toward future-proofing our setup. In our atom-membrane coupling experiment the interaction is mediated by an optical lattice. Primarily, this means that the size of our atomic sample will be determined by the very light responsible for the coupling, rendering the mode matching point mute. Furthermore, the appropriate waist of our lattice is determined by the need for its axial frequency, set to match the frequency of the membrane via the power, to stay roughly constant over the expanse of the atom cloud.

1.2.3 Geometry of the Atom Cloud

With equations 1.10 and 1.11 we can write

$$U_{\mathrm{dip}} = U_0 \frac{1}{1+\frac{z^2}{z_R^2}} \exp\left(-2\frac{r^2}{w_0^2\left(1+\frac{z^2}{z_R^2}\right)}\right), \tag{1.12}$$

separating out the terms that determine the spacial form of the potential. The Taylor expansion of this expression around $r^2 \ll w_0^2$ and $z^2 \ll z_R^2$ gives $U_{\mathrm{dip}} \approx U_0\left(1-\frac{z^2}{z_R^2}\right) \times$

$\left(1 - \frac{2r^2}{w_0^2}\left(1 - \frac{z^2}{z_R^2}\right)\right)$, which, to second order in r and z, reduces to

$$U_{\text{dip}} \approx U_0 \left(1 - \frac{2r^2}{w_0^2} - \frac{z^2}{z_R^2}\right). \tag{1.13}$$

As always $r^2 = x^2 + y^2$, so in the centre of the trap the dipole potential is well approximated by a 3D-harmonic potential with cylindrical symmetry. To define trap frequencies ω_r and ω_z we can equate this expression to the standard form of the harmonic oscillator,

$$-U_0 \left(\frac{2r^2}{w_0^2} + \frac{z^2}{z_R^2}\right) =: \frac{1}{2}m\omega_r^2 r^2 + \frac{1}{2}m\omega_z^2 z^2. \tag{1.14}$$

Now, a comparison of coefficients yields,

$$\omega_r = \sqrt{\frac{-4U_0}{mw_0^2}}, \qquad \omega_z = \sqrt{\frac{-2U_0}{mz_R^2}}. \tag{1.15}$$

The thermal spacial density distribution of atoms in a harmonic trap is Gaussian in all directions [22]. Using cylindrical coordinates and exploiting the symmetry in the transverse direction we can write,

$$n(r,z) = N_{at}\sqrt{\frac{1}{8\pi^3\sigma_r^4\sigma_z^2}}\exp\left(-\frac{r^2}{2\sigma_r^2}\right)\exp\left(-\frac{z^2}{2\sigma_z^2}\right), \tag{1.16}$$

where $\sigma_i = \omega_i^{-1}\sqrt{k_B T/m}$. Assuming isotropic temperature we find that almost all parameters drop out of the aspect ratio,

$$A := \frac{\sigma_z}{\sigma_r} = \frac{\omega_r}{\omega_z} = \sqrt{2}\,\frac{z_R}{w_0} = \sqrt{2}\,\frac{21.3\,\text{mm}}{85\,\mu\text{m}} = 355. \tag{1.17}$$

While this expression for the aspect ratio is probably most intuitively useful as it relates common atomic size parameters to the common size parameters of the laser beam it can be simplified to

$$A = \frac{\sqrt{2}\,\pi}{\lambda} w_0, \tag{1.18}$$

as the Rayleigh range is also a function of the beam waist. This reveals that a larger beam waist elongates the atom cloud, further justifying our moderation in the choice of its value. Figure 1.4 shows the size of the atom cloud as a function of its temperature, anticipating the relevant scale.

An issue raised by the diffraction-considering model in [41], again for the case of a simple probe beam, is that when atom clouds become too elongated the coupling strength depends only on the 3D peak atomic density. They determine that the length of the atomic sample must be compared to a quantity they call the modified atomic Rayleigh range and define by

$$\tilde{z}_R = \frac{\pi w_0^2 \sigma_r^2}{\lambda_{\text{probe}}(w_0^2 + \sigma_r^2)} = \frac{z_R}{1 + w_0^2/\sigma_r^2}. \tag{1.19}$$

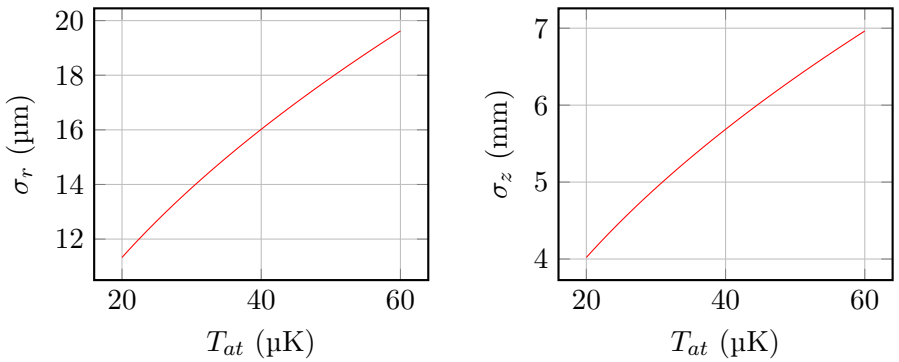

Figure 1.4: The predicted rms-size parameters of the atom cloud, assuming a thermal ensemble in a harmonic trap, plotted against temperature.

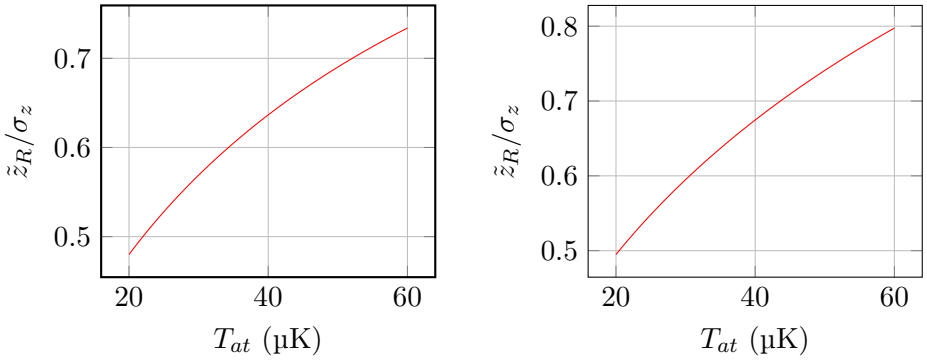

Figure 1.5: On the left, $\tilde{z}_R/\sigma_z$ is plotted for a probe beam of the same size as the atomic sample (mode matched to first order). On the right the probe beam has a waist of $w_0 = 115\,\mu\text{m}$, like our 1D optical lattice.

The scaling transitions in the limit $\sigma_z \gg \tilde{z}_R$. Fortunately, as shown in figure 1.5, our case is not so extreme, and diffraction effects can be corrected for with geometrical factors.

Chapter 2

Characterisation of the Dipole Trap

This chapter collects all the information and data pertaining to the dipole trap itself. Section 2.1 describes building and loading the dipole trap; sections 2.2-2.4 detail all the characterising measurements conducted, including atom temperature, trap lifetime, trap frequency, trap depth, and the OD of the atom cloud. For quick reference, the values of all these parameters are collected in appendix A.

2.1 Experimental Setup

Our light source is a Mephisto MOPA laser made by InnoLight.[1] Its power output is 42 W at 1064 nm. At this high power it is necessary to work with components specifically designed to withstand it without damage.

As described in section 1.1.1, the vacuum cell where atoms are trapped is on a raised breadboard. For clarity, the setup on each level is shown separately: the level of the optical table in figure 2.1, and the level of the breadboard in figure 2.2.

The beam is focused to an initial waist of 225 µm by the laser's internal optics a few millimetres inside its enclosure. The beam is first directed through a Faraday isolator to prevent possible back reflections from reaching and damaging the laser. About 30 cm of space are required before the isolator to let the beam expand and reduce its intensity to avoid exceeding the isolator's damage threshold. Next, a combination of a half-wave plate and polarising beam splitter cube (PBS) is used to reduce the power in the beam manually for alignment purposes. An aperture is placed after the PBS to block light scattered by the small cube. A telescope focuses the beam through an acousto-optical modulator[2] (AOM), which directs the zeroth-order into a beam dump. Finally, the first order beam is directed to a periscope to raise it to the breadboard level. On the level of the breadboard the beam is focused onto the position of the atoms with a $f = 200$ mm lens. Dichroic mirrors,[3] placed on either side of the vacuum cell, overlap the beams of the dipole trap and the optical lattice described in chapter 3.

[1] InnoLight have since been acquired by Coherent, but these same lasers are still produced.
[2] AOMO 3110-197 by Gooch & Housego
[3] DMLP950 by Thorlabs, Inc.

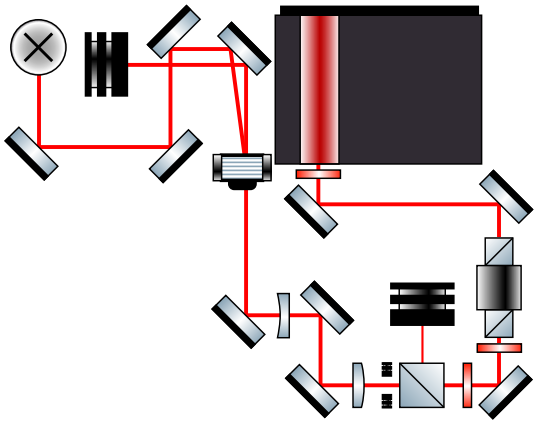

Figure 2.1: The setup of the dipole trap on the level of the optical table.

Symbol	Meaning
	Half-wave plate
	Faraday isolator
	Beam dump
	Open aperture
	AOM
	Periscope
	Dichroic mirror
	Vacuum cell

Table 2.1: A legend listing uncommon symbols.

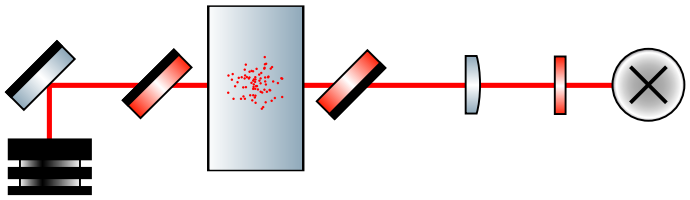

Figure 2.2: The setup of the dipole trap on the level of the breadboard.

These mirrors reflect light at 780 nm and transmit light at 1064 nm with up to 99.5% efficiency when the light is appropriately polarised. In particular, p-polarised light is favourable in transmission and s-polarised light is favourable in reflectance.

2.1.1 Beam Shaping and Profiling

The theory of dipole trapping as discussed in section 1.2.1 is valid for a Gaussian beam in the spacial TEM_{00} mode. Specifically, our design considerations relied heavily on the assumption that the beam's intensity profile is given by equation 1.10. To ensure that this is reasonably accurate, to measure the beam waist, and to discover possible drifts in the beam's position we image a cross-section of the beam with a beam profiler.[4] The beam quality and its spacial mode are of special concern, as the setup is entirely in free space without mode cleaning.

When a beam passes through a correctly aligned AOM what happens to it depends on the beam waist. A well known trade off is between the rise time and the diffraction efficiency. When a beam's waist is small it takes less time for the phonons in the AOM crystal to stop interacting with the light, and thus the rise time is shorter than it would be for a larger beam. In turn this smaller interaction region leads to lower diffraction efficiency. While some manufacturers comment on it [43], it is rarely a concern and therefore seldom mentioned that passing through an AOM with a small

[4] WinCamD-UCD12 by DataRay Inc.

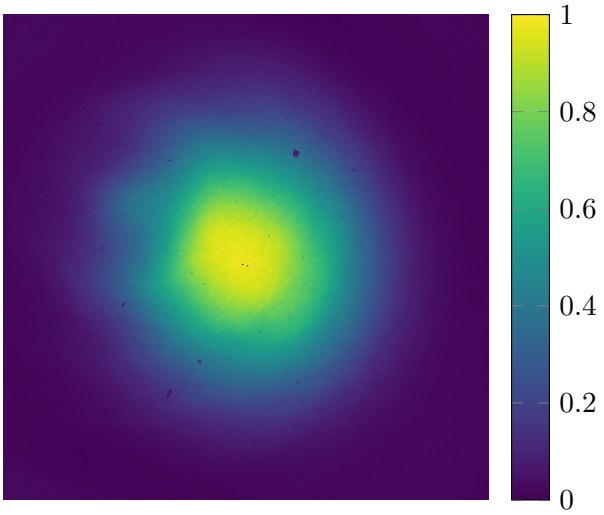

Figure 2.3: In this image, the first order beam after the AOM is shown. Colour maps to normalised intensity. The size of the image is 400×400 pixels, where one pixel is $4.65\,\mu m \times 4.65\,\mu m$. Through iterative optimisation the beam is made as circular after the AOM as when first emitted by the laser, and measured to be in the desired Gaussian mode to 98%. During the optimisation process attention was paid to the beam's mode shape and ellipticity, exclusively varying the beam waist at the AOM. The first order beam after the AOM showed an ellipticity, defined as the ratio of the diameters of the minor and major axes, of up to 0.7. Additionally, sometimes a mode that most resembled TEM_{10} was observed, as would be expected for the zeroth order.

beam waist can degrade the beam quality, increasing ellipticity, or even producing strange mode shapes. On the other hand, beams that are too large will partially miss the acoustic beam, lowering diffraction efficiency again, or even clip on the finite-sized device aperture, lowering beam quality. Specifically, the aperture of the AOM is circular with a 3 mm diameter, but it performs to specification (i.e. the laser beam fully overlaps the acoustic beam) when the laser is incident within the "active aperture", which is a rectangle of size $2.5\,mm \times 1.25\,mm$. The only way to be sure all is working as intended is to look at the beam directly.

For these reasons the lenses of the telescope and AOM positions had to be iteratively tested and optimised. Eventually, it turned out that the best results were achieved for a beam with a $1/e^2$ diameter close to the size of the smallest side of the AOM's active aperture. Thus our telescope, consisting of a plano-convex lens with $f = 250\,mm$ and a plano-concave lens with $f = -200\,mm$, focuses the beam to $w_0 = 550\,\mu m$ at the position of the AOM. In the optimisation procedure beam waists down to about $w_0 = 300\,\mu m$ were tested. The final shape of the beam after the AOM is shown in figure 2.3. The diffraction efficiency is 73%.

To gain further insight into the beam shape at the position of the atoms, where

direct access is no longer possible, a mock setup with equivalent propagating distance and a thick piece of glass to mimic the vacuum cell was constructed. With this setup it was first determined that, for a $f(\lambda = 1064\,\mathrm{nm}) = 229\,\mathrm{mm}$ focusing lens, the beam waist of the dipole trap at the position of the atoms is about 92 µm. The value output by the camera is the geometric mean value, meaning it is the radius of a circle with the same area as the beam. This measurement comes with an uncertainty that is unrelated to the setup merely imitating the real experiment. The waist determined by the camera is a function of the exposure time, giving results differing by 5 µm to 10 µm in the worst case depending on whether the automatically determined safe exposure time is approached from above or below. Measurements were always taken after approaching the safe exposure time from below to ensure some internal consistency, but this strange effect reduces the overall trustworthiness of the measured values.

Indirect measurements of the beam waist via the trap depth and frequency in the actual setup are presented in section 2.4. Those measurements have the advantage of being performed on the real setup and are in close agreement with each other. The value obtained from measuring the trap frequency, $w_0 = 85\,\mu\mathrm{m}$, is used in the calculations because it stems from the more sensitive measurement. The measured trap depth suggests $w_0 = 82\,\mu\mathrm{m}$.

For investigating the possibility of thermal lensing, the power in the laser beam is reduced manually (i.e. with a half-wave plate and a polarising beam splitter) directly before the dichroic mirror. The beam position varies on the order of 10 µm between low and high powers at the position of the atoms. In the even more realistic case of setting the power with the AOM this effect may worsen, as thermal effects in the AOM's crystal also come to bare. Fortunately, no obvious drifts take place when the power is kept constant. Therefore, while it may be necessary to realign optics when changing the power in the dipole trap, drifts due to thermal effects should not be an everyday issue, and in particular they are unlikely to cause a problem within the course of a single experimental run.

2.1.2 Loading the Dipole Trap

For traps near resonance, scattering photons from the trapping light on the trapped atoms is an important source of heating and often the dominant atom loss mechanism. The photon scattering rate for a two level atom in the RWA [22] is given by,

$$\Gamma_{\mathrm{scat}} = \frac{\Gamma U_{\mathrm{dip}}}{\hbar \Delta}. \tag{2.1}$$

This yields a rate around 1 Hz, which is far too low to contribute significantly to the loss of atoms from the trap. Despite previously noting the inaccuracy of the RWA for very large detuning we need not seek a more accurate expression for such a small effect. The relative error introduced is a few tens of percent, but even if our estimate were off by an order of magnitude the effect would still be negligable. Over 10^3 scattering events are required to heat an atom out of the trap, but as we will see in section 2.2.3, the background gas collisions already limit the trap lifetime to 10 s.

In principle, scattering photons is not the only way the dipole potential could adversely affect the temperature of the atoms. Its light shift could deteriorate the laser cooling performance. In turn, it may be possible to compensate this effect through optimisation of the laser frequencies in the relevant stages of the MOT. Fortunately, an initial comparison of the MOT cooling with and without the dipole trap turned on during all the early stages found little difference. We decided to keep the dipole trap laser on during all the MOT phases to maximise its loading time and avoid all potential issues with pointing and switching on time. Subsequently, the laser frequencies during the MOT phases were also optimised.

Loading efficiently means that it is necessary to cool atoms from the initial temperatures in our MOT to below the trap depth of the dipole trap. As the MOT is initially large and spherical, and the dipole trap is narrow and highly prolate, the overlap between the two traps is small, and the MOT must be compressed as much as possible just to bring atoms into the correct spacial region to be captured by the dipole trap. Further, as atoms begin to be captured by the dipole trap, it is critical to avoid scattering them back out of it. The details of optimising loading have been studied, for instance in [21], yielding, essentially, a check list of loading steps and the most important parameters to look out for in each of them.

In our experimental sequence there are four phases designed to load the dipole trap. In order these are MOT loading, dark MOT, weak MOT, and molasses. All of them were reoptimised to yield the greatest number of atoms transfered. Prior versions of these phases are fully characterised in [18]. During MOT loading the 3D-MOT is continuously loaded by an atom beam from the 2D-MOT. The process takes 3 s and the resulting cloud contains around 5×10^9 atoms at a mild 5 mK. In the dark MOT phase the 2D-MOT is switched off, the detuning of the 3D-MOT light is increased, and the intensity of the repumper is reduced over 100 ms. This reduces the scattering rate of the cooling light, which results in a compression of the atom cloud. In the weak MOT phase the MOT light is detuned ever further to the red and the magnetic field gradients are turned down reducing the confinement. Over another 100 ms the atom cloud cools from 2 mK at the end of the dark MOT phase to just 200 µK. Finally, for 13 ms in the molasses phase the magnetic field gradients are switched off completely. Measurements show that the atoms do not get colder in this phase, so at first glance it is strange that it has a positive effect on the number of atoms loaded into the dipole trap. While some further investigation may be warranted, it is plausible that this phase simply moves more atoms into the dipole trap for geometric reasons.

The modifications made from the sequences decribed and characterised in [18] are very minor. Some of the most important parameters of each phase, i.e. the laser-atom detuning, the magnetic field gradients, and the intensities were quickly scanned and tweaked to optimise the number of atoms loaded into the dipole trap after turning everything else off for 100 ms to let all the free atoms fall away. Few changes were necessary, as the existing sequence was designed for a similar task. Through this tweaking the number of atoms in the dipole trap after 100 ms could be improved from just under 10^7 to 3×10^7 in the best case. In addition to the MOT parameters, once many atoms are loaded into it, holding the dipole trap for a few seconds and

locating the centre of the atom cloud allows an accurate determination of the position of the focus of the beam. This enables optimal positioning, and reliably detects when decreased performance is due to optics needing realignment.

2.2 Temperature, Atom Number, and Lifetime

Absorption imaging is a highly suitable and powerful technique to interrogate an atom cloud for its properties. This method, described in section 1.1.2, gives qualitative information about the imaged atomic ensemble, and when it is appropriately calibrated quantitative information about the cloud's temperature, the number of atoms it contains, and its density distribution. For this reason, this section must begin by briefly discussing imaging. Our imaging system sends a beam through and around the atom cloud, whose shadow is imaged onto a CCD with a single lens. The dipole trap is long and narrow and it would be quite a coincidence for a system designed to image the large MOT to just happen to image the correct plane for the dipole trap to be in focus. Further, its position determines the position of the optical lattice, so it is doubly important for the imaging system to image this plane. When the imaging lens is slightly off from the proper position the atom cloud appears blurred. This is a subtle effect to catch with the naked eye. We noticed the problem due to another effect at the edges of the atom cloud at short times-of-flight, around (100 µs), when imaging with detuned light. The atom cloud appears to split in two at the edges. The effect is asymmetric in detuning indicating that its nature is dispersive, and that the atoms are acting as a lens.

The side-view imaging system is still set up generally as described in [18], however the position of the lens imaging the atoms onto the camera's CCD had to be adjusted. As the imaging system uses only a single lens, this modification necessarily changed the magnification. The imaging lens is held in a lens tube with extended threading, which makes it possible to move the lens by screwing and unscrewing its mount. According to specification, the distance between threads is 0.635 mm. Thus, a positioning accuracy of almost 1/10 mm can be achieved simply by marking off quarter turns on the lens tube, which is sufficient for accurate focusing. While it may seem a little improvised, this method actually has numerous advantages over the "high-tech" solution of mounting the lens on a translation stage. Firstly, a translation stage would need to be clamped down separately from the camera, which happened to be an issue in our case because of limited space and a hole in the breadboard for bringing up MOT light from the optical table below. Secondly, a translation stage introduces another degree of freedom in proper alignment. Thirdly, a translation stage is inferior to a lens tube in protecting both the lens from dust, and the camera from stray light.

To focus the imaging system, we exploited the same effect that first let us notice something was amiss. When the image is properly focused, the splitting of the atom cloud at the edges disappears. With persistence, a little bit of fine tuning can be achieved by additionally minimising the waist of the atom cloud, but the real changes are small and the shot-to-shot variations are at least as large. When the focus is

finally satisfactory, gravity serves as a scale bar for determining the new magnification, as the cloud falls at a known rate. After our adjustments each of the camera's $6.45\,\mu\text{m} \times 6.45\,\mu\text{m}$ pixels corresponds to $14.46\,\mu\text{m} \times 14.46\,\mu\text{m}$ in the image plane, a magnification of 0.446.

2.2.1 Theory: Time-of-Flight and Loss Mechanisms

To determine the temperature of an atom cloud through absorption or fluorescence imaging, a method called time-of-flight or TOF was developed. The trapping light is switched off abruptly and the cloud is allowed to expand freely for a time t_{TOF}. For an initially Gaussian distribution under ballistic expansion the final distribution of the cloud can be found through convolution with the velocity distribution [44]. The final form along a direction x is a new Gaussian distribution,

$$n(x, t_{\text{TOF}}) = \frac{N}{\sqrt{2\pi}} \frac{1}{\sqrt{\sigma_x^2 + \sigma_t^2}} \exp\left(-\frac{x^2}{2\left(\sigma_x^2 + \sigma_t^2\right)}\right), \tag{2.2}$$

where $\sigma_t = t_{\text{TOF}} v_{\text{rms}}$ and everything else is as in equation 1.16. A series of measurements of the total width along r, $\sigma = \sqrt{\sigma_r^2 + \sigma_t^2}$, where r means any direction orthogonal to z, for varying values of t_{TOF}, yields a data set linear in t_{TOF}^2. Concretely,

$$\sigma^2(t_{\text{TOF}}^2) = \sigma_r^2 + v_{\text{rms}}^2 t_{\text{TOF}}^2. \tag{2.3}$$

Then the temperature can be extracted from the velocity with the defining equation for temperature from kinetic gas theory, $T \coloneqq \frac{m v_{\text{rms}}^2}{k_B}$.

The final temperature of atoms in a dipole trap is determined by a balancing of evaporation and heating processes, wherein heating is a small effect and evaporation becomes small as the atoms get colder. Evaporation was studied theoretically and experimentally in great detail in the nineties because of its importance in achieving Bose-Einstein condensation [45, 46]. Although it is now an established and well known technique, it continues to be a source of interesting optimisation problems today [47]. Kinetic theory gives a picture of a Maxwell-Boltzmann distribution of atoms truncated at the trap depth repeatedly, until the temperature is so much lower than the trap depth that the effect becomes negligible. To reach the temperatures required for Bose-Einstein condensation, this process is encouraged by lowering the trap depth as atoms cool, so that the potential they experience is always shallow. This is called forced evaporation. The parameter that describes how deep or shallow a trap appears to atoms is the ratio of the trap depth to the temperature of the atoms, $\eta = |T_d|/T_{at}$. The choice of η when using evaporation to cool is critical, but as runaway evaporation depends on the collision rate remaining constant or increasing as atoms evaporate their confinement is just as crucial. This can mean that the optimisation to achieve high efficiency when the trapping potential is ramped down must deliberately consider the changing trap frequencies as well [47]. Alternatively, there are methods that decouple trap depth and confinement, and achieve fast and efficient evaporation in that way [48]. As we are not changing the trap depth for now, we will reach a steady state temperature

somewhere in the "deep trap regime", which typically means $10 \geq \eta \geq 6$ [49, 50]. The scaling laws in [49] can be used to estimate the time constant of evaporation, incorrectly assuming a constant η, to be on the order of seconds. Finally, evaporation also means losing atoms. Evaporation is the dominant loss mechanism initially, but only a fraction of the trapped atoms will actually evaporate. Once the deep trap regime is reached the lifetime of the atoms is instead limited by collisions with the background gas.

Collisions with the background gas are the ultimate end of all sufficiently long-lived dipole traps. The lifetime is inversely proportional to the pressure of the background gas, but also depends on the species composition of the gas. While the exact cause is unknown the pressure measurements made during the initial setup of the vacuum chamber were not entirely conclusive [23]. We can however take the measured MOT lifetime around 10 s as a prediction and lower bound for the background gas limited lifetime.

2.2.2 Temperature Measurements

To evaluate the temperature a series of absorption images is taken and processed with a program called MatCam, written by Caspar Ockeloen [51]. MatCam can automatically fit Gaussian distributions to the atom cloud and saves the widths and positions in x and y. When the distribution of the atoms is approximately Gaussian, the inclusion region around the atom cloud is selected properly, and the signal to noise ratio is not too small, then this program accurately guesses initial values to produce fits of high goodness. A devil's advocate might conversely argue, that when MatCam fails to produce a nice fit of a regular atom cloud, then the data is too poor to be fit without giving an unreasonable amount of influence to the person producing the fit. As an additional check, the atom number can be determined through this fit and compared to the number independently obtained from the OD. As the latter is a fairly direct measurement discrepancies speak against the quality of the fit.

An atom cloud's density decreases as it expands freely. That the OD must not be too large for absorption imaging to be quantitative was briefly discussed in section 1.1.2, but the opposite is also true, as the difference between the image and the reference becomes comparable to the noise level for sufficiently low OD. For this reason the most reliable, reproducible TOF results are achieved when t_{TOF} is kept short and the number of data points is made reasonable by using a small step size. Our data are taken at $t_{\mathrm{TOF}} \leq 4\,\mathrm{ms}$, with $\Delta t = 100\,\mu\mathrm{s}$. Some representative examples are shown in figure 2.4.

Combining many TOF measurements for different hold times of the dipole trap reveals the time evolution of the temperature in the cloud. These data are shown in figure 2.5. As is expected for cooling due to evaporation, the data are explained well by the function

$$T(t) = T_{\mathrm{evap}} \exp\left(-\frac{t}{\tau_{\mathrm{evap}}}\right) + T_f. \tag{2.4}$$

The fit yields an initial temperature of $T_i = T_{\mathrm{evap}} + T_f = 54\,\mu\mathrm{K}$, a final temperature of $T_f = 34\,\mu\mathrm{K}$, and a characteristic time of evaporation $\tau_{\mathrm{evap}} = 1.9\,\mathrm{s}$.

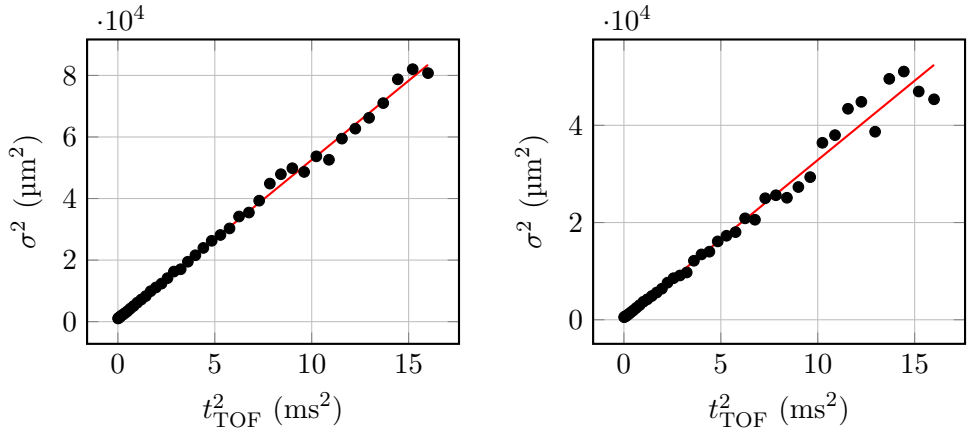

Figure 2.4: TOF data for the dipole trap. The extremes of the hold times were chosen as examples. On the left, the dipole trap is held for 100 ms before being released; on the right the hold time is 10.1 s. The fitted temperatures are 54 µK and 34 µK respectively. The significant decrease in atom number increases the spread in the data for the longer hold times, slightly lowering the SNR for the longest values of t_{TOF}.

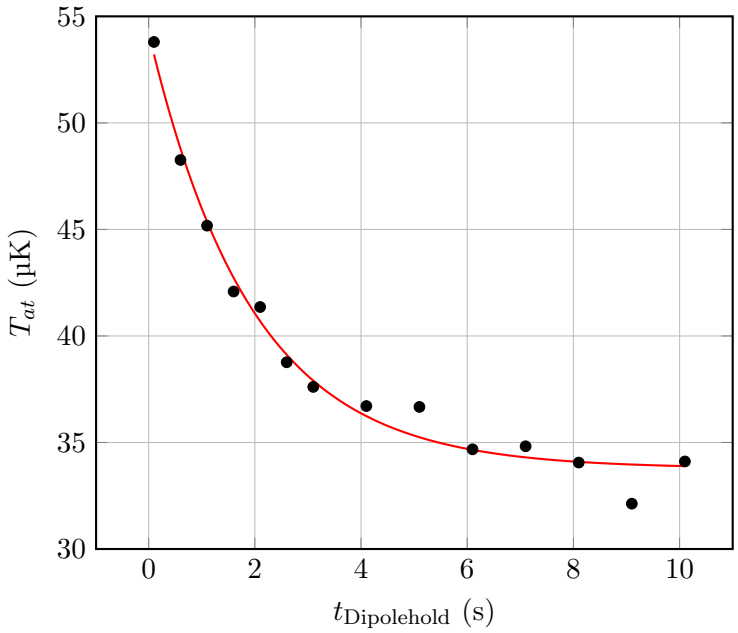

Figure 2.5: The temperature in the dipole trap is fit with a single exponential decay modelling the effect of evaporation. The first data point is taken after 100 ms to let all the free atoms that are present initially fall away. The step size is half a second initially and increased to one second after $t_{\mathrm{Dipolehold}} > 3\,\mathrm{s}$.

In principle, it is also possible to extract a value for σ_r from time-of-flight data to compare to the calculations shown in figure 1.4. Unfortunately, the spread of these values is quite large. This is to be expected due to the similarity of the effective pixel size, 14.46 µm, and σ_r, which also makes estimating σ_r from a single picture taken after a short TOF difficult. These TOFs yield a mean value of $\sigma_r = 21$ µm but the data range from 10 µm to 30 µm, and the scatter is such that the expected dependence of σ_r on T_{at} is lost.

2.2.3 Atom Number and Lifetime Measurements

As discussed in section 2.2.1, the number of trapped atoms decreases over time due to two main loss mechanisms, evaporation and collisions with the room temperature background gas. As shown in figure 2.6, these separate effects can be distinguished from the data, which are fit better when allowing for two independent loss processes. The model that best explains the data thus has the form

$$N_{at}(t) = N_{\text{evap}} \exp\left(-\frac{t}{\tau_{\text{evap}}}\right) + N_{bg} \exp\left(-\frac{t}{\tau_{bg}}\right). \tag{2.5}$$

From the fit the total number of trapped atoms is $N_{at}(0) = N_{\text{evap}} + N_{bg} = 4.4 \cdot 10^6 + 1.7 \cdot 10^7 = 2.2 \cdot 10^7$ and the lifetimes of the processes are $\tau_{\text{evap}} = 1.1$ s and $\tau_{bg} = 12.4$ s. The evaporation caused lifetime is comparable to, but shorter than the characteristic time of evaporation from the previous section. This makes sense qualitatively, as more atoms are lost to evaporation while the atom cloud is warmer.

As η changes over time, the rate of evaporation is initially much faster than what is suggested by extrapolating the data in figure 2.6 to times shorter than 100 ms, and it is safe to say that the number of atoms lost to evaporation is underestimated. If the atom number in the dipole trap could reliably be determined in the first 100 ms, then the additional data points would make the curve in figure 2.6 much steeper for hold times between 0 ms and 100 ms. This is evident from the fact that the first, highest temperature measurement of the atoms in the dipole trap is 54 µK, which means the atoms are already fairly deep in the trap with $\eta = 5$. In contrast, the last, coldest temperature measurement of the atoms in the MOT is 200 µK, which, if they were all trapped in the dipole trap, would yield $\eta = 1.4$. Many of these MOT atoms are just in the wrong place to be trapped, but some unknown amount are definitely trapped at that temperature and lost to evaporation while it still occurs quickly. While slightly shorter times can be probed, there is no good substitute for gravity that would remove atoms free at $t_{\text{Dipolehold}} = 0$ s from the picture more quickly and allow accurately determining the number of atoms that evaporate from the dipole trap.

The rates of these loss processes do not depend explicitly on the number of trapped atoms. It is therefore not so important how quantitatively accurate the measurement of N_{at} is in order to state the lifetime. However, a quantitatively accurate measurement of the number of trapped atoms is important in terms of its relation to the density and the OD, and unfortunately many factors influence the quality of that measurement.

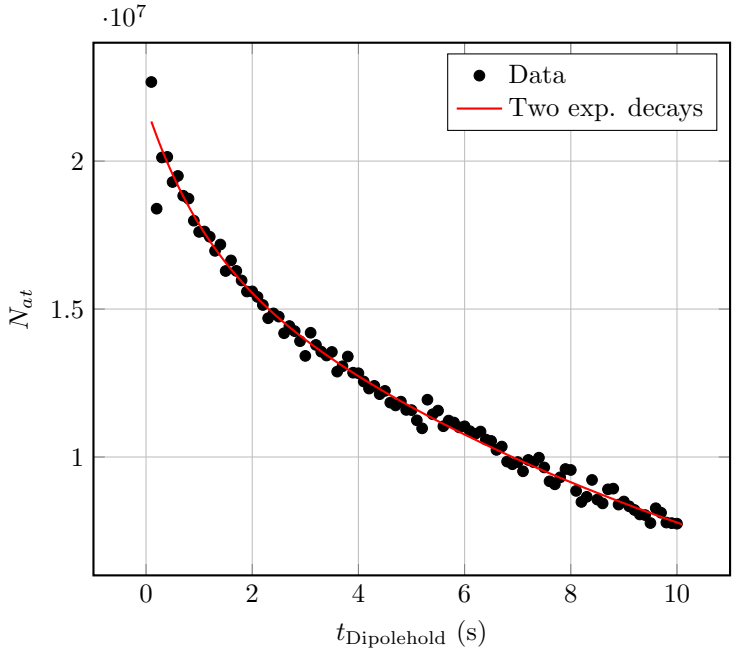

Figure 2.6: The lifetime measurement in the dipole trap requires a fit of two exponential decays to accurately capture the initial steepness of the curve. This approach is justified by the two known loss processes limiting the lifetime of the trap, namely evaporation and background gas collisions.

An issue that can affect N_{at} are drifts in the optics of the dipole trap that alter the position and alignment of the beam and reduce how many atoms are loaded into the trap over time. Further, as can be seen in the spread of the data in figure 2.6, there are shot to shot variations in N_{at} of a few percent. Aside from periodic realignment, we are also looking into a fibre solution for the dipole trap to improve the beam's pointing stability, but of course at $P \geq 21\,\text{W}$ this requires special equipment. There are also apparent effects. A slightly out-of-focus imaging system, as discussed in section 2.2, can cause an inconsistency between the measured value of N_{at} and the value of N_{at} from the best fit Gaussian density distribution. There may be slight imperfections in the polarisation of the imaging light, or in the alignment of the small B-field required to define the quantisation axis for imaging, or the number of scattered photons may be too small, all of which can worsen the accuracy of the measurement of N_{at}. The imaging system is calibrated to account for these issues with an effective reduction in scattering cross section $\sigma_{\text{eff}} = \sigma_0/\alpha$. From this calibration a systematic error of 10 % remains on measurements of the atom number [18].

2.3 Optical Depth

High optical depth was a key motivating factor in building this dipole trap. To gain some insight into this, consider the expression that is derived in [52] for $\bar{n}_f$, the min-

imum phonon occupation number of a membrane in a cavity coupled to an atomic ensemble. This is the number that determines whether interesting quantum mechanics, such as state swaps, can be done with the membrane or not. In [18] it is shown, that the terms of $\bar{n}_f$ are inversely proportional to the quantum cooperativity between the membrane and the atoms, and that, in the absence of optical losses, this reduces to

$$\bar{n}_f \propto \frac{1}{C_{qu}} = \frac{1}{C_m C_a} = \frac{1}{C_m OD_{res}}. \tag{2.6}$$

Here C_m is the light-membrane cooperativity and C_a is the light-atom cooperativity corresponding to the resonant OD of the atoms. Similarly, in our quantum memory experiment, the efficiency improves with optical depth. For instance, it was calculated in [10] that for an OD of 500 a storage efficiency of 82% can be achieved on the D_1 line for single photons from a quantum dot source.

2.3.1 Theoretical On-axis OD

To begin, we combine equations 1.2 and 1.16 and perform the integration over z to get

$$OD_{res}(r) = \frac{\sigma_0 N_{at}}{2\pi\sigma_r^2} \exp\left(-\frac{r^2}{2\sigma_r^2}\right) \tag{2.7}$$

We also define the peak resonant optical depth as $OD_{p,r} = OD_{res}(r = 0)$. In the case of our 1D optical lattice the polarisation is linear, so the expression for σ_0 is not the same as for the circularly polarised imaging light. Instead we use $\sigma_0 = \frac{\lambda^2}{\pi} \approx 1.94 \times 10^{-13}\,\mathrm{m}^2$ [28] which is valid for linearly polarised light in the rest of this section. This spacial profile of the optical depth is plotted in figure 2.7.

Considering the peak OD and reducing the expression to terms we have some direct experimental control over we have $OD_{p,r} \propto PN_{at}/T_{at}w_0^4$ (or $OD_{p,r} \propto N_{at}/w_0^2$ after the temperature reaches its steady state value). This expression lies at the heart of the tricky optimisation problem of increasing the optical depth. At first glance, this equation suggests much is to be gained in minimizing the beam waist, but this is somewhat misleading because the atom number is also some function of w_0, and because smaller waists increase the technical difficulty of using the high OD. Further, as the beam waist decreases so does z_R, reducing the homogeneity of the sample and thus how much of it is useful. Leaving the beam waist and power fixed we return to the issues of efficient loading and precooling to minimise evaporative losses. Using the empirical expressions for the time dependencies of the temperature and atom number, given in equations 2.4 and 2.5 respectively, we can plot the theoretical temporal evolution of the peak optical depth in our experiment as is. This is shown in figure 2.8.

2.3.2 On-axis Absorption Imaging

In addition to the side-view imaging system, two further imaging systems described in [18] are available. The first was originally designed to image the atoms in a 1D optical lattice, along its axis, onto a photo diode. The imaging beam had originally

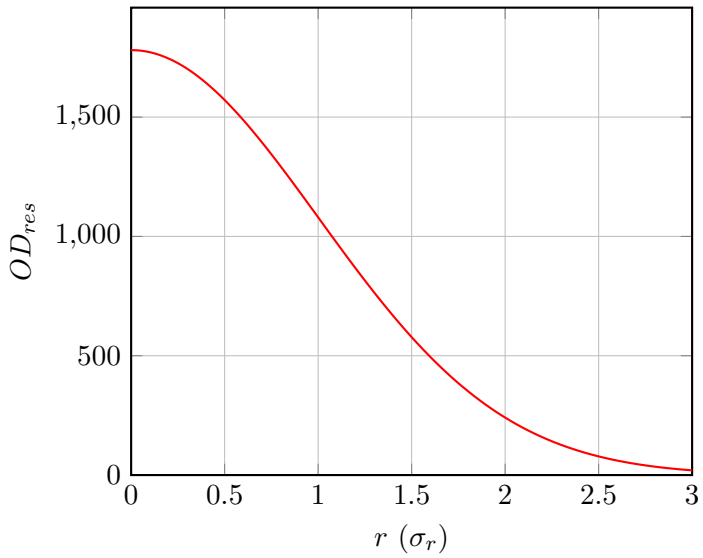

Figure 2.7: The spacial profile of the OD plotted for $N_{at} = 2 \times 10^7$ and the theoretical value of σ_r at $T_{at} = 54\,\mu\text{K}$, which approximates the experimental situation at $t_{\text{Dipolehold}} = 100\,\text{ms}$.

been mode matched to the lattice beam, resulting in a waist of 305 µm. As the PD effectively integrates the intensity over the area of the imaging beam, to measure the OD of the atom cloud the imaging beam would have had to be modified to match its mode, which is a daunting task without spacial resolution. The second imaging system originally imaged along an axis at a 22° angle to the main axis, onto a second CCD camera[5] (imaging 2a in [18]). This camera was repositioned to image along the axis in an attempt to measure the on-axis OD of the atom cloud.

The camera pixel size is 5.6 µm × 5.6 µm. An $f = 200\,\text{mm}$ lens and an $f = 400\,\text{mm}$ lens are used to achieve a magnification of 2. With an AOM, the detuning of the imaging light can be varied up to a maximum detuning around -11Γ. Because of the limits of absorption imaging discussed in section 1.1.2, this means that the maximum resonant OD that can reliably be measured is around

$$OD_{res,max} = \left(1 + \frac{4\Delta_{max}^2}{\Gamma^2}\right) \times OD_{max} \approx \left(1 + 4 \times 11^2\right) \times 3 = 1455. \tag{2.8}$$

An image taken at these settings is shown in figure 2.9. While the OD may well be too high to determine accurately, clearly more is happening in this image. At $t_{\text{Dipolehold}} = 100\,\text{ms}$ the full length of the cloud at the $1/e^2$ level is $4\sigma_z \approx 27\,\text{mm}$, which is a large object to focus on simply considering the required depth-of-field. Conversely, as can be seen, the cloud is sufficiently small radially to cause diffraction. This combination of effects gives rise to a blurry image, full of interference patterns, that probably misrepresents the contrast too.

[5] Guppy Pro F-031B by Allied Vision Technologies GmbH

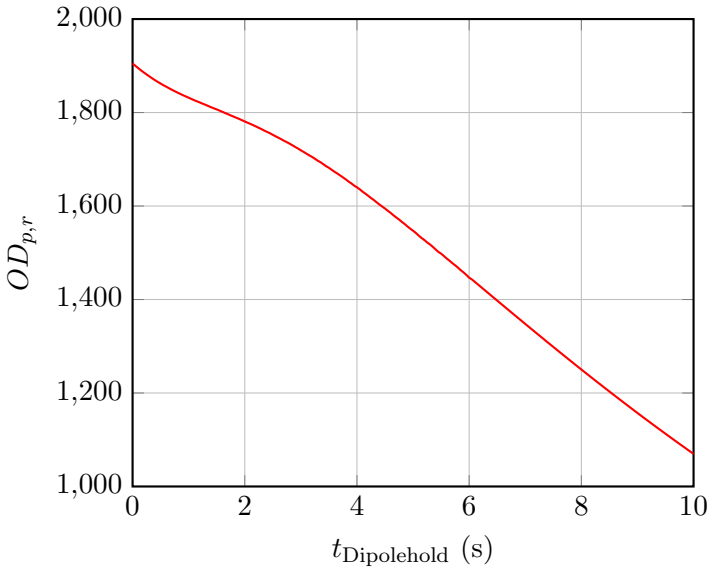

Figure 2.8: The evolution of the peak OD of our atomic sample over time, extrapolated from temperature and atom number data.

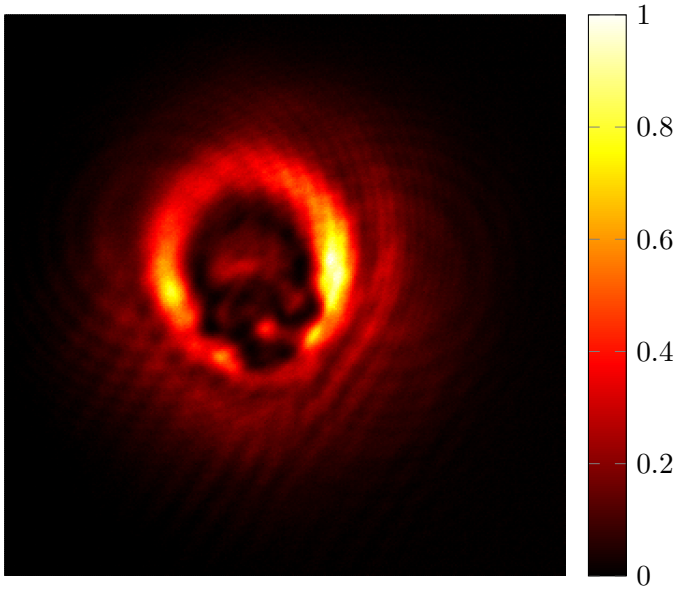

Figure 2.9: This absorption image is taken after 100 ms hold time with the highest available imaging detuning, around 11 times the natural linewidth. The colour maps to normalised intensity. The size of the image is 300×300 pixels, the real size of one pixel is $5.6\,\mu\text{m} \times 5.6\,\mu\text{m}$, and the magnification is 2. The imaging light is still blocked so strongly that the measured OD when this image is compared to a reference image is up to 5, and higher than 4 for many pixels, resulting in a mostly saturated central region.

These problems lead us to consider a number of possible alternatives. The simplest solution, requiring almost no change to the setup, is to use a laser that can be detuned further from the imaging transition as the source of the imaging light. However, this may require a careful investigation into how strongly the transitions from and to other states in the hyperfine manifolds are and can be suppressed, with preparatory optical pumping, even more careful alignment of the imaging magnetic field, and cleaning the polarisation of the imaging beam, to get accurate data. Baring that, polarisation contrast or Faraday imaging has been demonstrated as a method for cancelling diffraction while imaging dense clouds [53]. Alternatively, it would be possible to image the atom cloud from above and construct an on-axis image by combining a top-view and a side-view image taken with the main imaging system. These options remain open should a precise and independent determination of the OD turn out to be important, but both require some effort in implementing new imaging systems on the optical table and in our imaging software. A more pragmatic and imminently relevant approach is to conduct the coupling experiments that are our main interest anyway, and then to infer an effective OD from their results. Either way, the qualitative meaning of these results is clear even in the absence of reliable numbers; the peak on-axis resonant OD is definitely high.

2.4 Trap Frequencies and Trap Depth

There are two further independent characterising measurements that help paint a more complete picture of the system and reduce the reliance on calculated values. Firstly, measuring the trap frequency yields a way of determining the dipole trap's true beam waist consistently, without relying on beam profiling in a mock setup as was detailed in section 2.1.1. Secondly, measuring the light shift yields an empirical value for the trap depth and simultaneously reveals how well the imaging system is calibrated.

2.4.1 Transverse Trap Frequency Measurement

How trap frequencies can be measured depends on their magnitudes. To estimate them we can use equation 1.15, with the beam waist measured via beam profiling, $w_0 = 92\,\mu\text{m}$. These values yield $\omega_r = 2\pi \times 525\,\text{Hz}$ and $\omega_z = 2\pi \times 1.36\,\text{Hz}$. These values reveal that the motion of the atoms in r is on a time scale easily resolved by our cameras, which can image in time steps of $25\,\mu\text{s}$. However, ω_z is so low that finding a way to excite an oscillation that is not too strongly damped to be observed may be difficult. Additionally, the axial extent of the atom cloud is still too large for imaging its size or motion in z accurately, so we forgo a measurement of ω_z and focus exclusively on ω_r.

In a given dimension a displaced Gaussian in a harmonic trap displays a centre of mass oscillation at the trap frequency and a breathing oscillation at twice the trap frequency. One way to excite such an oscillation is to turn the trap off and on again after a short time. Some experimentation showed that ramping the trap down by linearly reducing the power over 1 ms also excited an oscillation while losing fewer

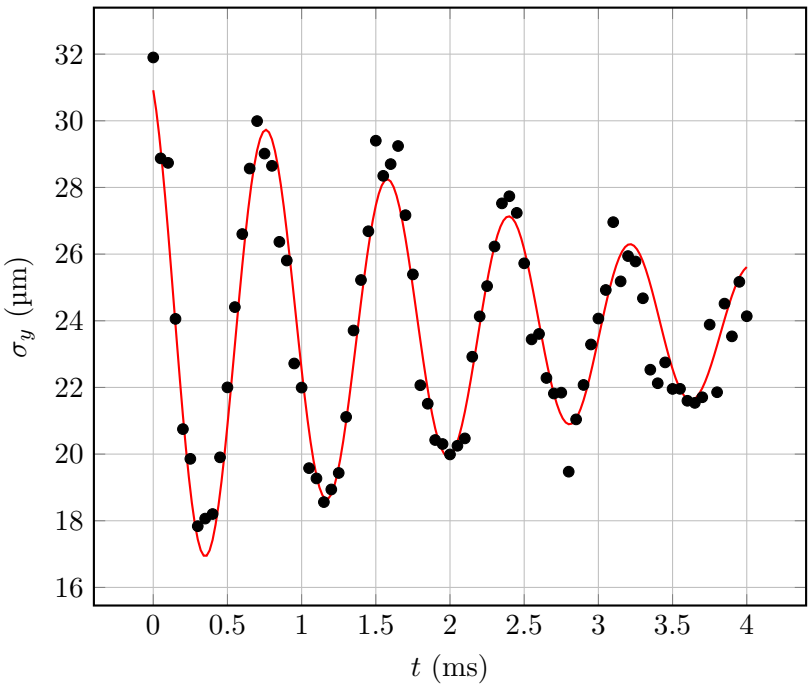

Figure 2.10: The excited breathing mode of the atoms in the dipole trap. The oscillation occurs at twice the trap frequency. The fit of this particular data set yields $\omega_r = 2\pi \times 615\,\text{Hz}$.

atoms leading to a better signal overall. The displacement the atoms have time to undergo is quite small, so the centre of mass oscillation cannot be seen. The breathing mode manifests itself in the width of the atom cloud, as shown in figure 2.10. With the average measured trap frequency of $\omega_r = 2\pi \times 611(5)\,\text{Hz}$ equation 1.15 can be rewritten as

$$w_0 = \sqrt{\frac{-4U_0}{m\omega_r^2}}, \tag{2.9}$$

to yield an alternative value for the beam waist. The result is $w_0 = 85\,\mu\text{m}$ as we have been using.

2.4.2 Light Shift Measurement

To measure the light shift, the frequency of the imaging beam is varied. We initially consider the typical case, where all trapping light is switched off before imaging. During regular operation, off resonant imaging results are automatically converted to resonant imaging results, as described in section 1.1.2, but here this step is omitted from the experimental sequence. Thus, while the true atom number is the same in each image, it will appear to be lower when the imaging beam is detuned from its transition. For

low saturation, the signal of absorption imaging is given by the Lorentzian [26, 54]

$$\mathcal{L}(\Delta) = \frac{1}{1 + \left(\frac{2\Delta}{\Gamma}\right)^2}, \quad N_{\text{measured}}(\Delta) = N_c \mathcal{L}(\Delta). \tag{2.10}$$

Here N_c is the true number of atoms in the centre of the cloud and Δ is the detuning of the imaging laser from the frequency of the bare imaging transition. Should a measurement reveal that N_c is actually measured for some non-zero value of Δ, the presence of a light shift is indicated. It is possible for a sub-optimal calibration to leave some remaining apparent light shift in the absence of trapping light, Δ_0, and in fact $\Delta_0 = -0.217\Gamma$ was found in the course of the following measurements. However, as it is a physically meaningless artefact of the calibration and mentioned only for completeness, this offset has been subtracted from all data for simplicity of presentation.

If the trapping light is now left on during imaging, then the light shift caused by the trap can be measured. As in the regular imaging procedure described in section 1.1.2, the atoms are briefly pumped into the $|F = 2, m_F = 2\rangle$ state before an image is taken. Over a series of images the frequency of the imaging beam is detuned to scan for a strong signal in the atom number. To first order, the light shift caused by the trap is simply the detuning that maximises the centred version of equation 2.10.

$$\mathcal{L}'(\Delta) = \frac{1}{1 + \left(\frac{2(\Delta + \Delta_0 + \Delta_{\text{LS}})}{\Gamma}\right)^2}. \tag{2.11}$$

The result of this measurement is $\Delta_{\text{meas}} = -1.70\Gamma$, as is shown in figure 2.11. In units of temperature this equals $-495\,\mu\text{K}$, which is far more than the value extrapolated for the trap depth from the trap frequency measurement in the previous section of $-280\,\mu\text{K}$.

Fortunately, there is a simple explanation for the discrepancy. What we measure here is not just the light shift experienced by the ground state, which is equal to the trap depth, but the sum of the light shifts of the ground and excited states. The dipole trap is so far detuned from the rubidium D_2 line that there are transitions available to the excited state from which the laser detuning is of a similar size, which can therefore produce a light shift of similar magnitude. The most significant of these are the D_2 line itself, i.e. $5P_{3/2}-5S_{1/2}$, but also $5P_{3/2}-6S_{1/2}$, $5P_{3/2}-4D_{5/2}$, and $5P_{3/2}-4D_{3/2}$. These transitions have been characterised with easy-to-use oscillator strengths, for instance in [35]. For a transition $5P_{3/2} - nI_J$ an associated oscillator strength f_{nI_J} can be used to determine the light shift with

$$\Delta_{5P_{3/2}} = -\frac{3\pi c^2}{2} I \sum_{nI_J} f_{nI_J} \frac{\Gamma_{nI_J}}{\omega_{nI_J}} \left(\frac{1}{\omega_{nI_J} - \omega_L} + \frac{1}{\omega_{nI_J} + \omega_L} \right). \tag{2.12}$$

Here Γ_{nI_J} is the classical decay rate given by Larmor's formula

$$\Gamma_{nI_J} = \frac{e^2 \omega_{nI_J}^2}{6\pi\epsilon_0 m_e c^3}. \tag{2.13}$$

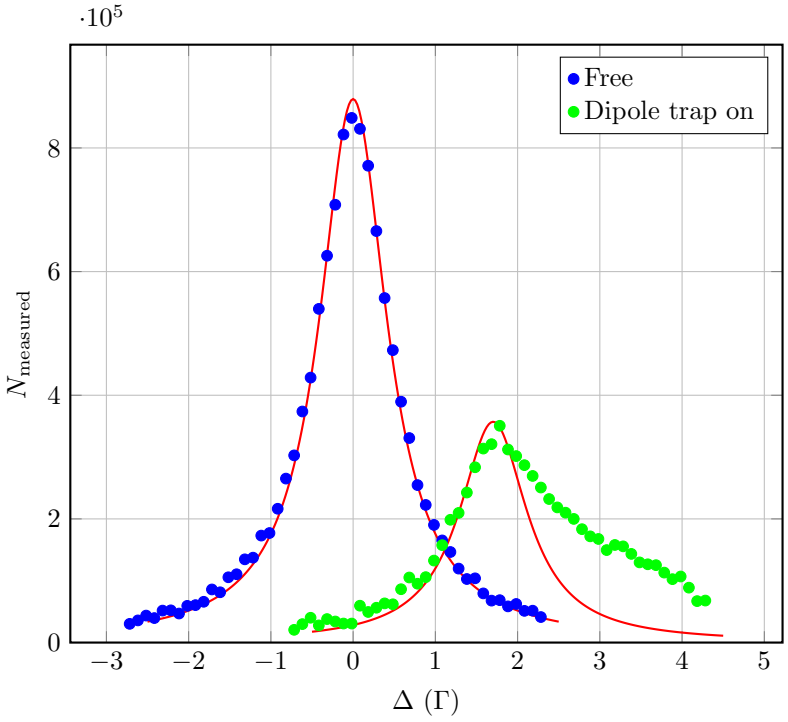

Figure 2.11: The light shift measurement for free atoms, and for atoms confined in the dipole trap. For convenience the imaging detuning is given in units of the natural linewidth, $\Gamma = 2\pi \times 6.065\,\mathrm{MHz}$. The long asymmetric tail of the data with light is probably due to imperfect polarisation of the probe beam or imperfect alignment of the imaging magnetic field. Such imperfections would lead to some probing of the π transition, i.e. $|F = 2, m_F = 0\rangle \rightarrow |F' = 3, m'_F = 0\rangle$, which experiences a strong light shift around $2\pi \times 64\,\mathrm{MHz}$ [55]. The data points in this tail were excluded from the fit. The measured light shift is $\Delta_{\mathrm{meas}} = -1.70\Gamma$.

This equation is completely analogous to equation 1.9, except that instead of a Clebsch-Gordan coefficient and a measured linewidth, an oscillator strength and a calculated linewidth are used. The relevant values of the transitions considered here are collected in table 2.2. This calculation can be combined with the ground state light shift to yield an expected total light shift in dependence of the trap depth of

$$\tilde{\kappa} = \kappa \frac{\Delta_{5S_{1/2}} + \Delta_{5P_{3/2}}}{\Delta_{5S_{1/2}}} \times \mathrm{MHz}\,\mu\mathrm{K}^{-1} \approx 36.9\,\mathrm{kHz}\,\mu\mathrm{K}^{-1} \tag{2.14}$$

where we have used equation 1.9 for $\Delta_{5S_{1/2}}$. A calculation considering 15 allowed transitions can be done to improve the accuracy of this value to $38.6\,\mathrm{kHz}\,\mu\mathrm{K}^{-1}$, which has also been measured successfully in circumstances similar to ours [55]. We can use this value to convert our measured light shift of 1.70Γ into a trap depth and find $T_d = 267\,\mu\mathrm{K}$.

Even though this measurement agrees well with the other results, we have so far

Transition	f_{nI_J}	λ
$5P_{3/2} - 5S_{1/2}$	0.7015	780.24 nm
$5P_{3/2} - 6S_{1/2}$	0.2032	1366.88 nm
$5P_{3/2} - 4D_{5/2}$	0.5888	1529.37 nm
$5P_{3/2} - 4D_{3/2}$	0.0654	1529.26 nm

Table 2.2: Recommended values from [35] for describing the most important transitions available to the $5P_{3/2}$ state.

neglected interesting physical effects that could change the value of the light shift. For instance, as the light shift is position dependent, the thermal motion of the atoms allows them to explore a region of the trap wherein the light shift is not constant. Thus, the measured signal is actually a convolution of the ideal signal and the distribution of the potential energy of the atoms. As the temperature is low in comparison to the trap depth, the region of the potential the atoms experience can be approximated harmonically. The distribution f_E of the total energy of a harmonic oscillator at a temperature T can be derived from statistical physics in the canonical, or microcanonical, ensemble. To this end, for the n dimensional harmonic oscillator with Hamiltonian

$$\mathcal{H}(\mathbf{q},\mathbf{p}) = \sum_{i=1}^{n} \left(\frac{p_i^2}{2m} + \frac{1}{2} m\omega^2 q_i^2 \right), \tag{2.15}$$

after the appropriate variable substitutions, the integral

$$f_E \propto c \int_{\mathcal{H}(\mathbf{q},\mathbf{p})\leq E} d^n q\, d^n p \exp\left(\mathcal{H}(\mathbf{q},\mathbf{p})/k_B T\right) \tag{2.16}$$

can be made to yield the famous scaling of $f_E \propto E^{n-1} \exp\left(-E/k_B T\right)$ [56]. For the potential energy on its own the same ansatz can be made. In that case the integration over p can be absorbed into the leading constant c. Its distribution is found to scale as $f_{E_{\text{pot}}} \propto E_{\text{pot}}^{n/2-1} \exp\left(-E_{\text{pot}}/k_B T\right)$, which is the same scaling as for a free particle with just kinetic energy. (Indeed for that case the integration over q can be carried out and absorbed into the leading constant.) As we are always interested in the distribution of the potential energy, we shall henceforth write $f_{E_{\text{pot}}}$ as f and E_{pot} as U. Specifically, in 3D, the distribution of the potential energy is

$$f(U,T) = \frac{2}{k_B T} \sqrt{\frac{U-U_0}{\pi k_B T}} \exp\left(-\frac{U-U_0}{k_B T}\right), \tag{2.17}$$

or in terms of frequency in units of MHz, temperature in units of µK, and using $\kappa = 10^{-12} k_B/h\,\text{K s} \approx 1/48$ as a dimensionless conversion factor,

$$f(\nu,T) = \frac{2}{\kappa(T/\mu\text{K})} \sqrt{\frac{((\nu-\nu_0)/\text{MHz})}{\pi\kappa(T/\mu\text{K})}} \exp\left(-\frac{((\nu-\nu_0)/\text{MHz})}{\kappa(T/\mu\text{K})}\right). \tag{2.18}$$

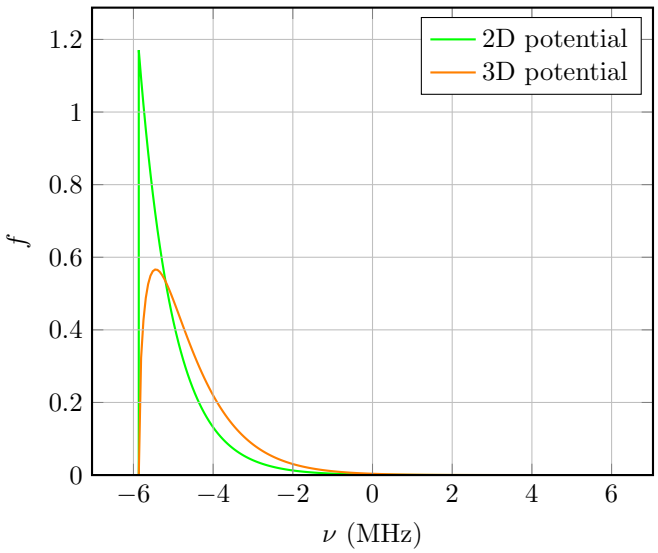

Figure 2.12: The normalised potential energy distribution in the dipole trap in 2 and 3 dimensions for $T_{at} = 41\,\mu\text{K}$, which is the temperature after 2 s hold time.

Note that these functions are defined to be zero for energies lower than the potential depth, U_0 and ν_0 respectively, where they would become imaginary.

It is intuitive that the more directions the atoms can move in, the greater the effect is on the light shift, and just that is the result of the statistical treatment of the dimensionality. This is why equation 2.10 was given in terms of a number of atoms in the center of the cloud. In reality it is not possible to restrict the imaging to the centre of the cloud in the transverse direction because the cloud is too small. It is however possible to restrict the imaging in z to reduce the effect to that of the 2D case. A Monte-Carlo simulation was run to verify that this strategy succeeds for a central region chosen to be narrow in comparison to z_R; the additional error was found to be negligibly small. The distributions for 2 and 3 dimensions are plotted in figure 2.12 for $T = 41\,\mu\text{K}$ and a trap depth of $-280\,\mu\text{K}$, which corresponds to $-5.83\,\text{MHz}$, and is expressed this way to match the units of Δ.

To find the effect f has on the light shift and to determine the signal function of absorption A, we perform the convolution

$$A(\Delta) = \int_{-\infty}^{\infty} \mathcal{L}'(-\Delta - \nu) f(\nu, T)\, d\nu\,. \tag{2.19}$$

Here the sign of Δ is flipped explicitly to enforce the conventions of trapping potentials causing negative light shifts which are then measured at a positive detuning of the imaging beam. To go beyond a symbolic representation, a specific temperature must again be chosen. The measurement here is conducted after a 2 s hold time, when the temperature is approximately 41 µK. The calculated signal for atoms at this temperature moving in 2 and 3 dimensions is compared with the calculated signal at zero temperature in figure 2.13. The result of the 2D case is $\Delta_f = -0.121\Gamma$. The 3D

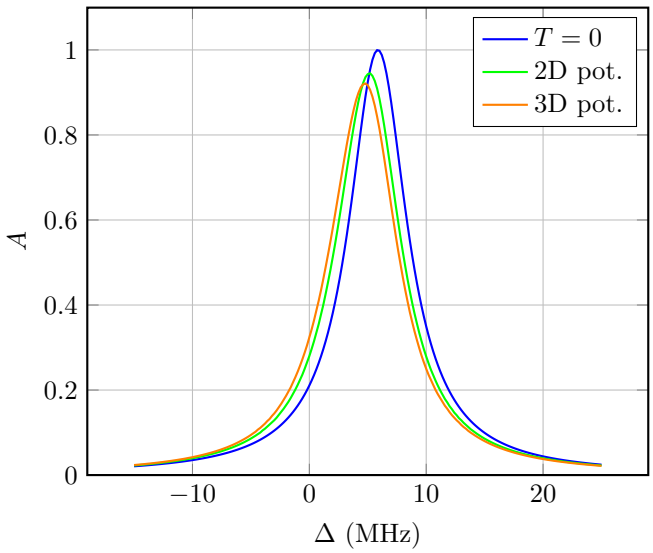

Figure 2.13: The expected signal from absorption imaging for atom clouds in 2D and 3D harmonic potentials at $T = 41\,\mu\text{K}$ during imaging, compared to the model without thermal effect. In the 2D case the peak response is shifted by $\Delta_f = -0.121\Gamma$. Only the ground state is considered here.

calculation is shown in addition to the 2D calculation because we will not be able to reduce our susceptibility to this thermal effect when we measure the light shift caused by the optical lattice in section 3.4.2. The effect of varying temperature is also further discussed there. Furthermore, the light shift of the excited state is also position dependent which modifies Δ_f. The final value of the correction due to thermal effects is

$$\tilde{\Delta}_f = \frac{38.6\,\text{kHz}\,\mu\text{K}^{-1}}{\kappa}\Delta_f = -0.214\Gamma. \tag{2.20}$$

Before we finalise our discussion of thermal effects on the light shift measurement with some numbers and comparisons, let us briefly discuss the effect of the atoms' velocity. Through the Doppler effect the light shift of the atoms is also influenced. If the velocities in the direction the imaging light is incident in are distributed with zero mean, as they should be, then they only cause a broadening of the signal rather than an offset. To further ease our minds, we check whether the shift would be significant if there were a preferred direction to the velocity. The frequency shift experienced by an atom with a velocity $\mathbf{v}$ due to the Doppler effect is just [24]

$$\Delta_{\text{Doppler}} = -\mathbf{k}\mathbf{v}. \tag{2.21}$$

Choosing the velocity and wave vector parallel and the velocity's magnitude to be the RMS value we can write,

$$\Delta_{\text{Doppler}} = -\frac{2\pi}{\lambda}\sqrt{\frac{k_B T}{m}}. \tag{2.22}$$

For $T = 41\,\mu\text{K}$ this works out to $-2\pi \times 80\,\text{kHz}$, which is a full order of magnitude smaller than $\Delta_f = -2\pi \times 732\,\text{kHz}$, even in this worst case scenario.

We can now adjust the measured value of the light shift to account for these thermal effects, $\Delta_{\text{LS}} = \Delta_{\text{meas}} + \tilde{\Delta}_f = -1.92(11)\Gamma$. The error margin is the combined statistical error of the two Lorentzian fits. Converting this light shift into a trap depth with the conversion factor $\tilde{\kappa}$ results in $T_d = -300(30)\,\mu\text{K}$, just a little higher than and still in agreement with the trap depth calculated from the trap frequency measurement of $T_d = -280\,\mu\text{K}$, although further away than the uncorrected value of $267\,\mu\text{K}$. The self-consistent beam waist required for this trap depth is $w_0 = 82\,\mu\text{m}$. Although the agreement is good, the trap frequency measurement is simpler physically and more sensitive. Specifically, to improve on the statistical error of the trap frequency measurement of $\pm 2\pi \times 5\,\text{Hz}$ the trap depth would need to be measured to $\pm 2\,\mu\text{K}$. For this reason values used in calculations are extrapolated from the trap frequency measurement.

Chapter 3

Characterisation of the Optical Lattice

This chapter describes the 1D optical lattice designed to couple the motion of a mechanical membrane oscillator to the motion of cold atoms [14]. It is the latest iteration of the coupling scheme used to study sympathetic cooling [16, 23] and self-oscillations [18] in this hybrid system. Theoretical details of the optical lattice are described in section 3.1. The experimental setup and loading procedure of the lattice from the dipole trap are the topic of section 3.2. Characterising measurements including atom temperature, lattice lifetime, trap depth, and frequencies are detailed in sections 3.3 and 3.4. As before, the values of all of these parameters are collected in appendix A for quick reference.

To implement loading this lattice from the dipole trap, instead of from the MOT, initially only foresaw the relatively minor change of reducing the beam waist in order to better match the dipole trap, and to preserve the qualities of the atomic ensemble generated therein. However, in the course of recharacterising the system, it became apparent that the tapered amplifier laser used initially had the unexpected and undesirable effect of heating the atoms, and had to be replaced by a titanium-sapphire laser. Further, we were hampered by successive, unforeseen technical issues. While these were all eventually overcome well enough to gain a thorough understanding of the system, and while characterising measurements show a quantifiable improvement over the previous setup, the results of a sympathetic cooling experiment with the membrane presented in chapter 4 still show signs of being limited in their quality by the implementation of the lattice. A discussion of what is still to be done is placed at the end of section 4.1.2.

3.1 Theory of 1D Optical Lattices

From the point of view of light-atom interaction, optical lattices and single-beam optical dipole traps are quite similar. Both use the dipole force to trap atoms via a position dependent light shift, and although the position dependence looks rather different in

the two cases, the mechanism is the same. Indeed both of these traps could accurately be called "(optical) dipole traps". To avoid confusion in this chapter and in the rest of this thesis the far off resonance single-beam dipole trap described in chapter 2 is consistently and uniquely called "the dipole trap", while the optical lattice is always referred to as the lattice. The most significant difference between our dipole trap and our optical lattice is the much smaller detuning from resonance with the atoms. The necessity of this is set by the membrane side of the experiment, which does not take kindly to the high powers required to achieve confining potentials far off resonance, and its needs determine many of the design choices concerning the lattice.

An important relation in that regard is the requirement $\omega_z = \omega_m$, i.e. that the axial frequency of the lattice matches the fundamental frequency of the membrane. In our case, $\omega_m = 2\pi \times 276.3\,\mathrm{kHz}$ [18]. Another is that by the very nature of the lattice being generated via reflection in the membrane cavity the atom-membrane interaction begins immediately. Once the lattice's frequency is high enough for sympathetic cooling the rate is on the order of kHz. This means that the behaviour of the optical lattice on time scales of 100 ms is interesting and important for understanding the system, and for eliminating the technical problems already alluded to, the relevant time scale for atom-membrane coupling is much shorter.

3.1.1 Derivation of Lattice Potential

To find the functional form of the intensity of the 1D optical lattice we describe its field as a superposition of incoming and reflected light fields $E_{\mathrm{lat}} = E_i + E_r$. Using classical light fields, setting $E_r = \sqrt{R}E_i^*$ where R is the intensity reflectivity coefficient, and showing some intermediate steps for clarity we can write the intensity as

$$\begin{aligned}
I(r,z) &= 2\epsilon_0 c^2 \left| E_i + \sqrt{R}E_i^* \right|^2 \\
&= 2\epsilon_0 c^2 \left| \frac{E_0}{w(z)} \exp\left(-\frac{r^2}{w^2(z)}\right) \left(\exp\left(-ikz\right) + \sqrt{R}\exp\left(ikz\right)\right) \right|^2 \\
&= 2\epsilon_0 c^2 \frac{|E_0|^2}{w^2(z)} \exp\left(-\frac{2r^2}{w^2(z)}\right) \left|\exp\left(-ikz\right) + \sqrt{R}\exp\left(ikz\right)\right|^2 \\
&= \frac{2P}{\pi w^2(z)} \exp\left(-\frac{2r^2}{w^2(z)}\right) \left(1 + R + 2\sqrt{R}\cos\left(2kz\right)\right) \\
I(r,z) &= \frac{2P}{\pi w^2(z)} \exp\left(-\frac{2r^2}{w^2(z)}\right) \left(1+\sqrt{R}\right)^2 \left(1 - \frac{4\sqrt{R}}{\left(1+\sqrt{R}\right)^2} \sin^2\left(kz\right)\right). \qquad (3.1)
\end{aligned}$$

The argument initially presented in section 1.2.1 to derive the ground state light shift caused by the dipole interaction of a single beam (equation 1.7) also applies for an optical lattice. In fact, because the lattice is linearly polarised and near resonance with the D_2 line, the situation is significantly simplified, allowing us to use the RWA

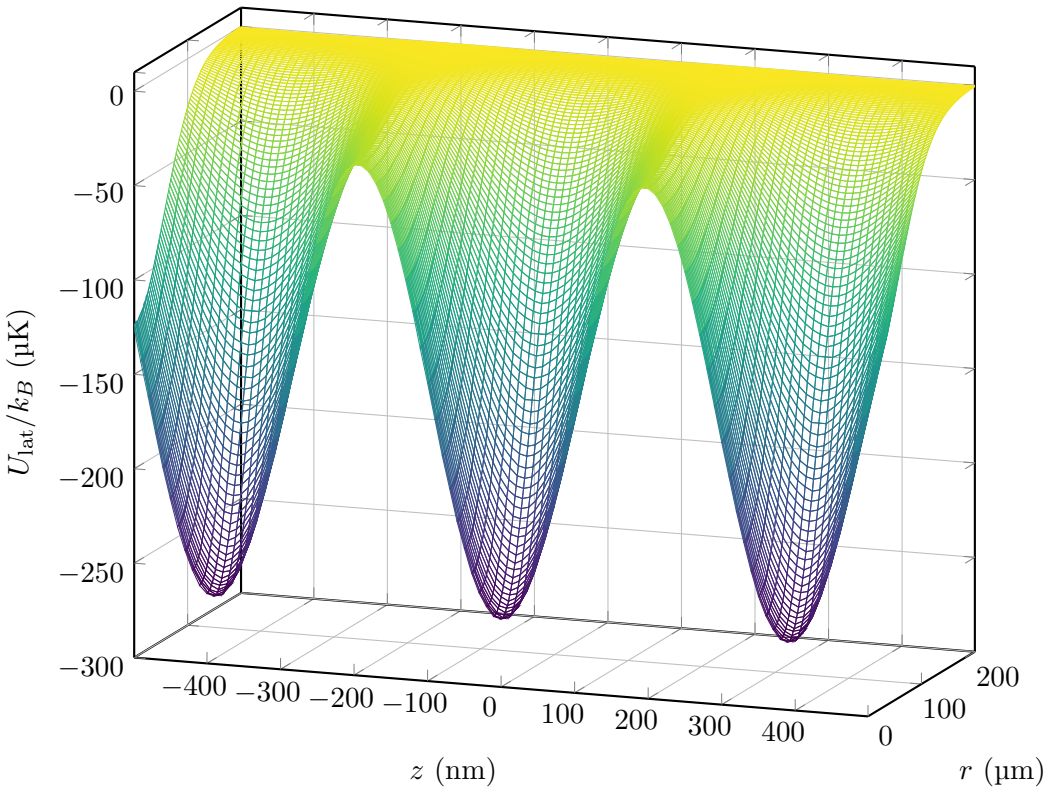

Figure 3.1: The lattice potential plotted for $P = 11\,\text{mW}$, $\Delta = -2\pi\times 40\,\text{GHz}$, $R = 0.25$, and $w_0 = 115\,\mu\text{m}$. At $r = 0$ the trap depth is modulated between $-264\,\mu\text{K}$ in the deepest troughs and $-29\,\mu\text{K}$ on the flattest peaks, effectively forming an array of 400 nm scale traps. As before, we define the convenient measure of the trap depth as $T_d = U_{\text{lat}}(r = 0, z = 0)/k_B$. On a scale where z becomes comparable to z_R a dipole-trap-like envelope becomes visible.

and neglect other transitions. This yields

$$U_{\text{lat}}(r, z) = \frac{\pi c^2}{\omega^3}\frac{\Gamma}{\Delta} I(r, z), \tag{3.2}$$

where ω, Γ, and Δ all refer to the D_2 line here and throughout this chapter when no subscript is given.

As we did for the dipole potential in equation 1.12, we can use equations 1.11 and 3.1 to separate the terms of the lattice potential with spacial dependence from those without (collected in V_0), arriving at

$$U_{\text{lat}} = V_0 \frac{1}{1 + \frac{z^2}{z_R^2}} \exp\left(-2\frac{r^2}{w_0^2\left(1 + \frac{z^2}{z_R^2}\right)}\right)\left(1 - \frac{4\sqrt{R}}{\left(1 + \sqrt{R}\right)^2}\sin^2(kz)\right). \tag{3.3}$$

Here V_0 is related to U_0 from equation 1.12 by $V_0 = \left(1 + \sqrt{R}\right)^2 U_0$. The Taylor

expansion of the lattice potential around $r \ll w_0$ and $\sin^2(kz) \ll 1$ to second order in r and z is given by

$$U_{\text{lat}} \approx V_0 \left(1 - \frac{2r^2}{w_0^2} - z^2 \left(\frac{1}{z_R^2} + \frac{4k^2\sqrt{R}}{\left(1+\sqrt{R}\right)^2} \right) \right). \tag{3.4}$$

For not too strongly focused beams $1/z_R^2 \ll k^2$, so the z^2/z_R^2 term is much smaller than the $k^2 z^2$ term and can also be neglected. Dropping the constant offset, using $k = 2\pi/\lambda$, and equating this expression to the standard form of a harmonic oscillator we find

$$-V_0 \left(\frac{2r^2}{w_0^2} + z^2 \frac{16\pi^2\sqrt{R}}{\left(1+\sqrt{R}\right)^2 \lambda^2} \right) =: \frac{1}{2} m\omega_r^2 r^2 + \frac{1}{2} m\omega_z^2 z^2. \tag{3.5}$$

A comparison of coefficients then yields the trap frequencies,

$$\omega_r = \sqrt{\frac{-4V_0}{mw_0^2}}, \qquad \omega_z = \sqrt{\frac{-32\pi^2 V_0 \sqrt{R}}{m\lambda^2 \left(1+\sqrt{R}\right)^2}}. \tag{3.6}$$

3.1.2 Scattering and Heating Rates

Neither the lattice potential nor the trap frequencies depend on power and detuning individually; instead both depend on the ratio P/Δ. In contrast, the photon scattering rate, given in equation 2.1, is proportional to P/Δ^2. As the spontaneous scattering of photons leads to heating, this is one of the most important arguments in favour of far detuned traps [22]. Unique to the case of optical lattices, fluctuations in the dipole force lead to a redistribution of photons between the travelling wave components. This effect can lead to strong heating in the resonant and near resonant cases and cannot be avoided by using blue detuned light [57, 58]. Fortunately, the strength of this effect falls off quickly with detuning and is negligable for $\Delta \geq 2\pi \times 1\,\text{GHz}$. Technical heating, specifically accidental parametric heating through laser noise [59, 60, 61], is another notorious source of heating. Following the insights gained in our efforts to heat parametrically to measure the axial trap frequencies, detailed in section 3.4.3, it does not appear to be a significant problem here. Instead, heating is dominated by the scattering of the trapping light on the atoms.

In a 3D harmonic trap, which we showed to be a good approximation for atoms at the bottom of each of the lattice's troughs, and neglecting possible anisotropy in the heating, the heating rate from scattering the trapping light is [22],

$$\dot{T} = \frac{T_{\text{rec}} \Gamma_{\text{scat}}}{3}. \tag{3.7}$$

Here Γ_{scat} is the photon scattering rate defined as in equation 2.1, but with the lattice potential in place of the dipole potential, $T_{\text{rec}} = \frac{\hbar^2 k^2}{m k_B}$ is the recoil temperature, and

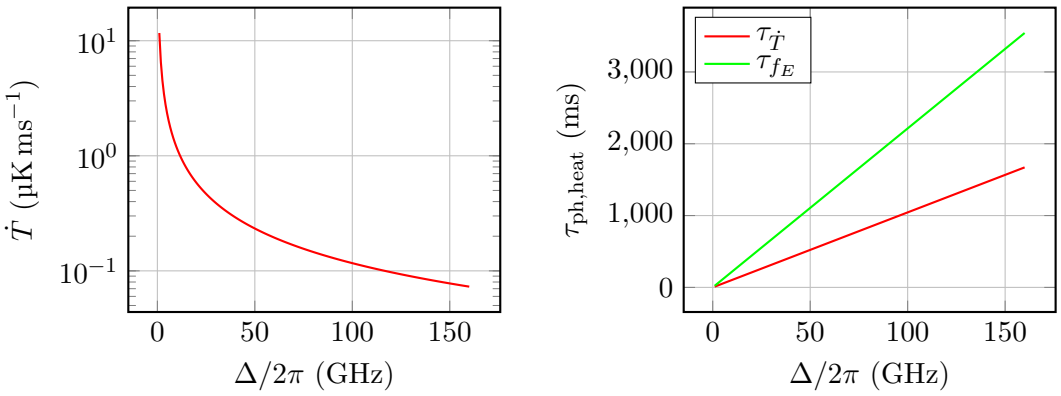

Figure 3.2: On the left, the heating rate due to scattering photons of the trapping light is shown, for a constant ratio P/Δ chosen so that $\omega_z = \omega_m$. On the right, two estimates of the lattice lifetime based on this heating rate are plotted. Note that both of these estimates are high upper bounds. Further, both calculations assume $w_0 = 115\,\mu\mathrm{m}$ and $R = 0.25$.

the factor 1/3 comes from the 3D harmonic nature of the trap. For rubidium at the lattice wavelength, $T_{\mathrm{rec}} \approx 360\,\mathrm{nK}$.

This heating rate considers only one temperature changing process, so it surely is an incomplete model of the thermal evolution of atoms in the lattice over time, but it does describe what we expect to be the most important heating mechanism. As such, it can be used to roughly estimate how quickly an atom can be heated out of the bottom of a lattice trough through scattering photons with

$$\tau_{\dot{T}} = -T_d/\dot{T}, \tag{3.8}$$

where $T_d = V_0/k_B$. This time gives a first estimate of the lattice lifetime. We can attempt to improve it by assuming that the atoms are thermally distributed in a harmonic trap, as in equation 2.18, with a time-dependent temperature. That is,

$$f_E(\nu, t) = \frac{2}{\kappa\left(T_i + \dot{T}t\right)}\sqrt{\frac{\nu}{\pi\kappa\left(T_i + \dot{T}t\right)}}\exp\left(-\frac{\nu}{\kappa\left(T_i + \dot{T}t\right)}\right). \tag{3.9}$$

We can further assume that the atoms begin deep in the lattice troughs by setting $\eta = 8$, which is where it ends up when the temperature reaches its final value in the dipole trap, and thus $T_i = T_d/8 = 33\,\mu\mathrm{K}$. Modelling the loss process with $N(t) = N_0 e^{-t/\tau}$, and defining "lost" as having a total energy $\nu + \kappa T_d > 0$, we can estimate the lifetime, τ_{f_E}, by finding how long it takes for the number of trapped atoms to be reduced to $1/e$ times the initial value. As is shown in figure 3.2, the relation between these lifetime estimates and detuning is linear when the ratio of P/Δ is kept constant. Unfortunately, this second estimate gives an even higher upper bound. The many other loss processes, some depending on detuning, some depending on temperature as hotter atoms are more easily lost to evaporation, and some, like background gas collisions, independent of both, will surely lead to much shorter actual lifetimes.

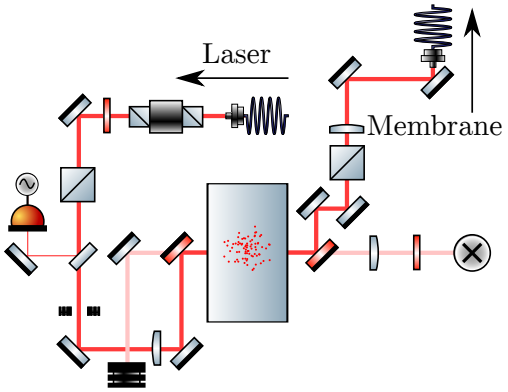

Figure 3.3: The setup of the lattice on the level of the breadboard extending figure 2.2. The lattice is drawn in red and the dipole trap is drawn in pastel pink.

Symbol	Meaning
	Fibre port
	Faraday isolator
	Half-wave plate
	Beam dump
	Beam Sampler
	Stabilisation
	Shutter
	Periscope
	Dichroic mirror
	Vacuum cell

Table 3.1: A legend for uncommon symbols used in figure 3.3.

3.2 Setup and Loading the Lattice from the Dipole Trap

The optical lattice is set up in three fibre linked parts. The beam is generated by a titanium sapphire laser[1] and passed through an AOM on the optical table, next to the setup for the dipole trap. After the AOM, the beam is coupled into an optical fibre and brought to the raised breadboard with the vacuum cell. After passing through the vacuum cell, another fibre brings the lattice light to a second optical table where the cavity containing the membrane is set up. There the light is reflected and brought back, forming a standing wave until it is stopped by the Faraday isolator placed immediately after the first fibre port on the breadboard. The level of the breadboard is shown in figure 3.3. For the contents of this chapter it is sufficient to imagine the fibre leading to the membrane as a mirror, that reflects about 25% of the incident light.

On the breadboard, some of the light is diverted to a photo diode to generate feedback for the AOM and stabilise the intensity. The intensity stabilisation box is homemade; more details on its design may be found in [62]. It prevents fluctuations in the lattice's trap frequency and thus in the optomechanical coupling. Placed immediately after this intensity stabilisation, a mechanical shutter can interrupt the beam within a few milliseconds via computer control. This shutter is important because the lattice needs to be completely off while the dipole trap is loaded, lest its light heats away most of the atoms. Using the AOM for this purpose, as was attempted initially, is a terrible idea. The time the AOM is off lets it cool, and upon switching the beam back on it takes several seconds for the set power to be reached. Additionally, because it is not possible to stabilise on zero intensity, the switching on behaviour caused by

[1] SolsTiS by M Squared

the intensity stabilisation is abrupt in this scenario, ruining all attempts at an adiabatic transfer of atoms from the dipole trap into the lattice. This configuration lets the AOM stay on with the shutter closed while the lattice is not needed. To turn the lattice on, the AOM is switched to a small power for the time it takes the shutter to open, about 1 ms, then when the shutter is fully open the AOM is ramped up to full power.

The setup of this lattice and the functionality surrounding it has been described in the previous experiments that relied on it [18, 23]. The most significant change to previous setups is that the former laser[2] was replaced and that all the optics were moved from one optical table to another. Care was taken to replicate each functional part of the existing setup. In particular, the homodyne detection system that reads out the membrane's oscillation amplitude [18] and also relied on light from the old laser was resupplied with light from the new laser. The breadboard level required some rearranging, the lenses for the lattice were replaced, a shutter was installed, and the first mirrors on either side of the vacuum cell were exchanged for their dichroic counterparts so that the lattice beam could be overlapped with the dipole trap beam. The final part, i.e. the cavity-membrane setup, remained effectively untouched.

3.2.1 Lattice Geometry, Design Choices, and Overlapping the Beams

The beam waist of the lattice is chosen to produce a reasonably homogeneous axial trap frequency. To limit the initial variation of the frequency to 10 %, the lattice's waist should be $w_0 = 2\sigma_r/\sqrt{-\ln(0.9)}$. Taking $\sigma_r = 18\,\mu\text{m}$ this yields a target waist of 110 µm. A second consideration is that in order to ensure that the atomic ensemble confined in the dipole trap is transferred to the lattice while maintaining favourable properties like the atom number and OD the lattice beam waist could be chosen to match $\omega_{r,\text{lat}}$ and $\omega_{r,\text{dip}}$. This would require a lattice beam waist of $w_0 = 98\,\mu\text{m}$. An $f = 200\,\text{mm}$ lens was chosen to focus the beam. An attempt at beam profiling was made, but because of the confined space on the breadboard sampling the beam and aligning the beam profiler perpendicular to the beam was tricky. The camera we use for beam profiling is quite sensitive to the angle of incidence, and a slight tilt can easily cause an error of a few microns in the beam waist measurement. The waist was measured this way to be around 100 µm.

One condition for the onset of sympathetic cooling of the membrane is that $\omega_z = \omega_m$. This fixes the ratio of P/Δ for the lattice without fundamentally fixing P or Δ. However, there is an optimal range for P for three important reasons. Firstly, more power is good because it increases the optomechanical damping rate, $\Gamma_{\text{opt}} \propto P$. However, at too high powers laser noise and optical absorption begin to limit optomechanical cooling. The effect can be modelled with a term increasing the bath temperature, T_L, with $T_L \propto P^2$ [16]. Thirdly, measurements of the membrane displacement spectrum show a number of noise peaks at frequencies just below the membrane frequency. Their source appears to be in the voltage supplies of the piezoelectric stages used

[2] TA Pro by Toptica

to position the components of the membrane cavity [18]. This effect currently limits the optomechanical performance of the cavity system. While the next generation of membrane setup may implement electrical filtering to combat this noise, for now it is important not to move the membrane frequency onto one of these noise peaks via the optical spring effect, where the frequency shift $\delta\omega_m \propto P$. In effect, this limits the usable powers to $P \leq 20\,\mathrm{mW}$. At $P = 11\,\mathrm{mW}$, which gives us a reasonable range to vary P, the detuning satisfying $\omega_z = \omega_m$, i.e. the maximum detuning for sympathetic cooling, is $\Delta = -2\pi \times 40\,\mathrm{GHz}$. Nevertheless, for characterisation and troubleshooting where longer lifetimes are important, we often used $P = 44\,\mathrm{mW}$ and $\Delta = -2\pi \times 160\,\mathrm{GHz}$.

Overlapping two beams with waists on the order of 100 µm is an iterative process. The beams can be overlapped by eye using an IR viewer card on either side of the vacuum cell. The distance available here is small as the beams are separated on the dichoric mirrors almost immediately on either side of the cell. Once some atoms are transferred, optimisation can be performed with reference to absorption images. In addition to the pointing degrees of freedom accessed by two mirrors there is also the issue of positioning the lens. For this purpose, the lens is mounted in a cage, with which its position in z can be adjusted. Unfortunately, it is not possible to align the beam sufficiently accurately without the lens to be fully independent of the lens position, as no atoms are trapped in the lattice unless the beam is focused. In other words, adjusting the lens significantly undoes other alignment work. While shot-to-shot fluctuations make it difficult to measure, it seems as though after thorough alignment, optimising on atoms transferred, no more than 5 % to 10 % of the atoms are lost in transfer. After alignment the overlap degrades slowly over time.

3.2.2 Lattice Loading Sequence

When to begin transferring atoms from the dipole trap to the lattice is the first question that must be answered. A transfer immediately after the MOT has fallen away would involve many atoms at a higher temperature, which may mean fewer atoms loaded deep in the lattice troughs. After around 3 s the atoms in the dipole trap have almost reached their final temperature but millions have been lost. A short hold time has the additional advantage of reducing the cycle time of the experimental sequence. Some different hold times for the dipole trap were tested, but no obvious advantage could be found in waiting longer than 100 ms. As we will see in the next section, the atoms are initially as cold as the final temperature in the dipole trap even so, which explains the lack of noticeable difference. Nevertheless, the hold time is a variable to keep in mind when this transfer process is tinkered with in future.

To load the lattice adiabatically, the potential must be increased slowly. This means, the steps in which the potential is turned on should be small in comparison to the temperature of the atoms, i.e. $\delta T_d \ll T_{at}$, and that the process should be slow in comparison to the trap frequencies confining the atoms. The latter condition is almost impossible to achieve axially because the dipole trap barely confines atoms in that direction. Indeed, slow in comparison to $\omega_{z,\mathrm{dip}}$ would mean an initial timescale of many seconds. The situation is further complicated by the fact that the interaction

with the membrane cannot be switched on and off independently of the lattice. In an atom-membrane coupling experiment whatever happens as the lattice intensity is ramped up will act on the membrane.

Additionally, while timescales are a concern, the condition of small changes relative to the temperature of the atoms is also an issue. In order to investigate the turning on behaviour of the AOM, a photo diode was placed just after the intensity stabilisation. Its output, viewed on an oscilloscope, let us observe the thermal effects of starting an AOM cold, first prompting us to install a shutter and make the default state of the AOM *on*. Once that technical issue was solved another notable effect appeared. If the light incident on the intensity stabilisation is too low to be measured accurately it generates an error signal and automatically increases the intensity. This manifests itself when ramping up from zero power as a short, fast initial increase in power, proportional to the set final value, but not exceeding about half that maximum. This occurs only when the initial power is low, but of course it is there that the effect is most significant.

For all these reasons the transfer process is implemented in three steps. The lattice ramp is primed by ramping from 0 mW to 1 mW while the shutter is opening, which takes about 850 µs. While U_{lat} is almost 24 µK at 1 mW the undesired response of the intensity stabilisation was found to behave best at this value. Adjustments to the stabilisation box itself were not yet made to attempt improving its behaviour, as such a change would also require monitoring the effect on the membrane. From 1 mW the lattice power is ramped again to its final value over 2 ms, after which the dipole power is ramped down to zero in another 2 ms.

The most significant possible improvements here lie in the first step of priming the lattice. A discussion of time scales could be interesting, but with the initial power of 1 mW the axial trap frequency is suddenly switched from $\omega_{z,\text{dip}} \approx 2\pi \times 1\,\text{Hz}$ to around $2\pi \times 80\,\text{kHz}$. Millisecond timescales for the rest of the transfer are slow with respect to that, but that hardly matters if many atoms are excited in the initial steps. From the perspective of the minimum outputs of our control system, we could ramp in steps two orders of magnitude smaller, which would satisfy $\delta T_d \ll T_{at}$ and thus could be called adiabatic. However, any attempts at optimisation here must be done in the context of a atom-membrane coupling experiment. If a changed setting on the stabilisation increases the noise on the membrane, or if a slow ramp obscures the coupling beyond analysis, then nothing is gained from improving the lattice loading process.

3.3 Temperature, Atom Number, and Lifetime

As briefly mentioned previously, this optical lattice is mainly tested for two sets of parameters. For those characterising purposes where a long lifetime is important $P = 44\,\text{mW}$ and $\Delta = -2\pi \times 160\,\text{GHz}$ are used, and to probe the lattice's properties more closely to the regime where it is used in atom-membrane coupling $P = 11\,\text{mW}$ and $\Delta = -2\pi \times 40\,\text{GHz}$ are used. Ideally the distinction is only important in this section, as trap depth and trap frequencies are determined only by the ratio P/Δ. Nevertheless, I identify for which parameters each data set was taken by stating the lattice power

or detuning, and unless directly specified otherwise this should be taken to mean that the other value was adjusted accordingly.

3.3.1 Temperatures and Heating Rates

Measurements of the temperature of the atoms in the lattice over time are shown in figure 3.4. For the case of the $P = 11\,\mathrm{mW}$ ($P = 44\,\mathrm{mW}$) lattice the measured heating rate is $0.083\,\mu\mathrm{K\,ms^{-1}}$ ($0.055\,\mu\mathrm{K\,ms^{-1}}$), low in comparison to the value calculated in section 3.1.2 of $0.65\,\mu\mathrm{K\,ms^{-1}}$ ($0.16\,\mu\mathrm{K\,ms^{-1}}$). This can be explained quite plausibly by evaporative cooling, i.e. the increased likelihood of hotter atoms being lost from the trap entirely. The scaling is not as predicted either, as the rates are almost the same for the two detunings despite the reasonable theoretical arguments for $\dot{T} \propto /\Delta$. This too is likely a result of atom loss depending on temperature.

For either detuning, the first temperature measurement at 10 ms yields a number just under 35 µK, which is almost 20 µK colder than the last measured temperature in the dipole trap before transfer. To assess whether this temperature change occurs because of evaporation it is appropriate to compare these data to the data from section 2.2. The initial atom cloud after 100 ms of holding the dipole trap is the same in the two cases. Additionally, as we will show in section 3.4, the trap depths of the dipole trap and the lattice after the completion of the transfer are highly similar, each around 280 µK. We find that in the case of the dipole trap this temperature decrease from regular evaporation takes a few seconds and involves the loss of about 5 million atoms, which is three orders of magnitude longer than the transfer takes and more than twice the number of atoms lost. Therefore, lacking viable alternatives, this cooling must occur due to some non-trivial mechanism during the transfer process. Studies of the entropy-temperature curves for bosons in optical lattices revealed that even fully adiabatic loading of a lattice can heat or, counterintuitively, cool atoms just through the compression of the system [63]. Thus, this lower initial temperature is not necessarily a sign for or against the loading process being adiabatic.

3.3.2 Lifetime Measurements

Before the laser was exchanged, a lot of strange data were produced in attempting to characterise this lattice. In addition to the temperature of the trapped atoms decreasing over time, lifetime measurements at various detunings all yielded the same value. The latter was the smoking gun evidence for the laser not behaving as we expected. The suspected cause is the amplified spontaneous emission (ASE) background of the laser. (The TA Pro is specified to a typical ASE background of −40 dB, which appears to be consistent with our measurements.) Of course, all the data shown in this chapter are taken using the new laser, as the goal is to characterise the system as it is to be used in atom-membrane coupling, but this noteworthy effect occupied sufficient time to be afforded a brief mention. The issue is not so much the level of ASE, but its broad spectrum, often spanning several nanometres. When attempting to work with a far detuned source, an ASE background, even at a level of −40 dB, means that a

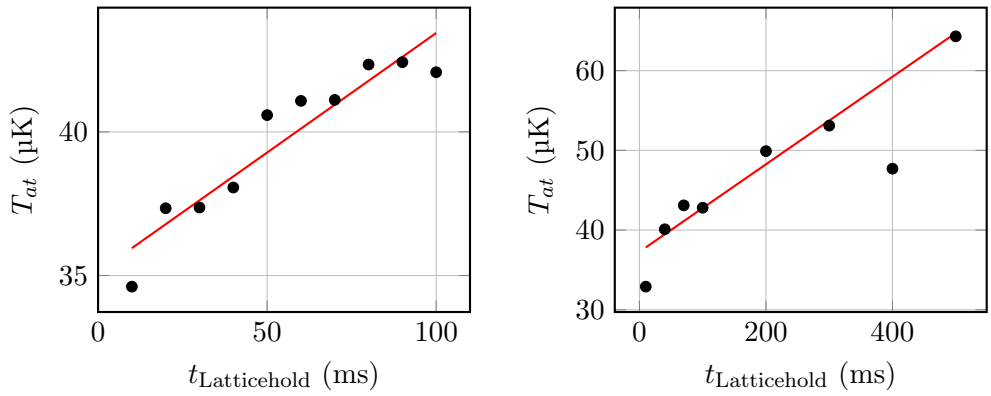

Figure 3.4: The temperature of the atoms in the lattice over time at $\Delta = -2\pi \times 40\,\text{GHz}$ (left) and $\Delta = -2\pi \times 160\,\text{GHz}$ (right). Note the differences in the scales. The heating rates are $0.083\,\mu\text{K}\,\text{ms}^{-1}$ and $0.055\,\mu\text{K}\,\text{ms}^{-1}$ respectively. In both cases the first measurement is after 10 ms. As the atom cloud is radially much smaller than the MOT was, free atoms fall far enough to be separated from it quickly, and measurements can be made soon after transfer without concern for counting any free atoms. The final temperature of the atoms in the dipole trap before transfer is 54 µK.

significant amount of light, in terms of P/Δ, is emitted near resonance.

Figure 3.5 shows the lattice lifetime measurements. As we expect there to be one dominant loss process, the data are fit with the model

$$N(t) = N_0 \exp\left(\frac{-t}{\tau}\right). \tag{3.10}$$

This yields $\tau = 76\,\text{ms}$ and $\tau = 270\,\text{ms}$ for $\Delta = -2\pi \times 40\,\text{GHz}$ and $\Delta = -2\pi \times 160\,\text{GHz}$ respectively, approximately replicating the linear scaling with detuning predicted in section 3.1.2. Note that the initial number of atoms here is on the same order as the number of atoms in the dipole trap at 100 ms, with no obvious drop due to transferring between the traps.

3.4 Trap Frequencies and Trap Depth in Partially Modulated Lattices

Partially modulated lattices, i.e. lattices with $R < 1$, behave a little differently from fully modulated lattices. For one, as can be seen in figure 3.1, when $R = 0.25$, at $r = 0$, there are about another $-29\,\mu\text{K}$ of potential depth giving radial confinement to the atoms even after they have escaped the lattice-like confinement in z. The exact value of R depends on two fibre couplings and the alignment of the end mirror. $R = 0.25$ is the typical value we strive for when reflecting off the cavity end mirror, but when coupling into the cavity properly we usually get closer to $R = 0.27$. Further,

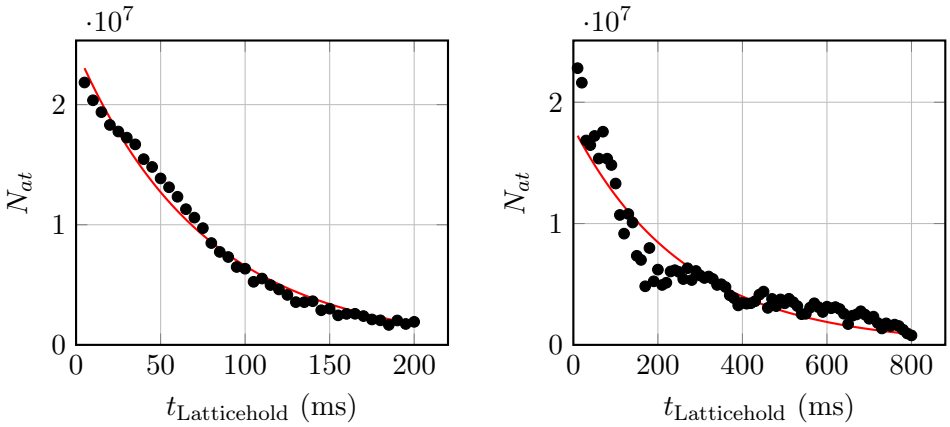

Figure 3.5: The lifetime of the lattice measured for $\Delta = -2\pi \times 40\,\text{GHz}$, shown on the left, and $\Delta = -2\pi \times 160\,\text{GHz}$, shown on the right. The $\Delta = -2\pi \times 160\,\text{GHz}$ data are of somewhat poorer quality as they are from an early characterising measurement, but the fitted lifetime could be confirmed by measurements after the system had been optimised.

the potential structure is such, that for $r \neq 0$ the confinement in z is also reduced. Moreover, because the incoming intensity is four times the reflected intensity there is a preferred direction for photon scattering, which is reflected in a movement of the atoms when they are able to overcome their confinement in z. These issues have proven to make some of these measurements more difficult than for the single-beam dipole trap. Therefore, some measurements are done in a single-beam configuration, meaning that the beam is blocked after passing through the vacuum cell instead of being back reflected. The resulting trap is just a single-beam dipole trap as described in chapter 2, but to distinguish this setup from the far off resonance dipole trap at 1064 nm I refer to it in this chapter as a lattice with $R = 0$, and use $R = 0$ and $R = 0.25$ as subscripts to distinguish the measurements made in these configurations.

3.4.1 Transverse Trap Frequency

To measure the transverse trap frequency of the lattice we proceed as in section 2.4.1. The expected value at $P = 44\,\text{mW}$, for a beam profiling measured waist of $w_0 = 100\,\mu\text{m}$, is $\omega_{r,\text{R}=0.25} = 2\pi \times 590\,\text{Hz}$. The result of the measurement is shown in figure 3.6, with a measurement at $R = 0$ for comparison. We interpret the nearly identical results of the two measurements as a sign of exciting the atoms out of the lattice's troughs by the very nature of the measurement in switching the lattice off and on suddenly. While the signal to noise ratio of these measurements looks quite good, attempts to reduce the strength of the excitation, for instance by ramping the lattice to half the full power instead of zero before snapping back on its normal power, failed to produce any viable or even identifiable signal. Other fractions of total power that were tried all either produced no signal, or a signal highly similar to that of the $R = 0$

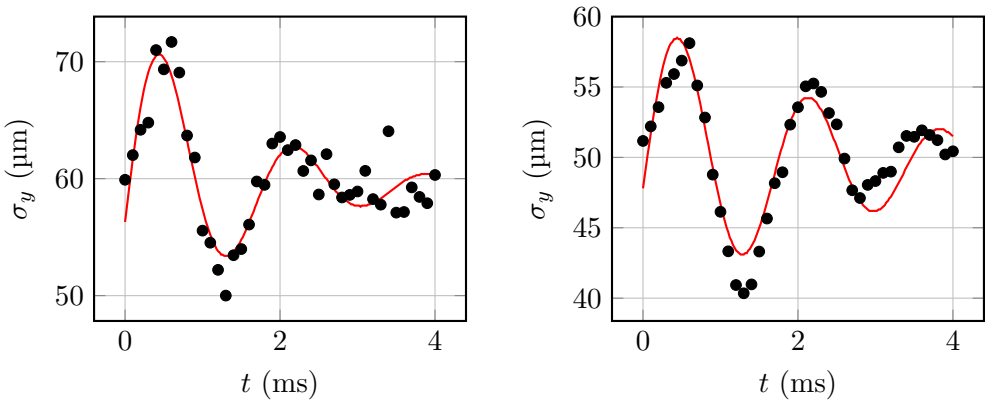

Figure 3.6: The excited breathing mode of the atoms in the $R = 0.25$ lattice is plotted on the left. The oscillation should occur at twice the trap frequency. The fit yields $\omega_{r,R=0.25} = 2\pi \times 288\,\mathrm{Hz}$, which is nowhere near the calculated value of $\omega_{r,R=0.25} = 2\pi \times 590\,\mathrm{Hz}$. For comparison the same measurement for the $R = 0$ lattice is shown on the right. The result is nearly identical, this particular data set yielding $\omega_{r,R=0} = 2\pi \times 296\,\mathrm{Hz}$.

case. To ensure that we actually do load atoms deep into the troughs we measure the light shift directly in the next section.

More so than for the dipole trap measurements in section 2.4.1, these oscillations are very noticeably damped. For the underdamped case of the harmonic oscillator,

$$x(t) = A \exp(-\gamma t) \sin(\omega t + \phi) + x_i, \tag{3.11}$$

which is our model, the measured frequency, ω, is related to the frequency of the undamped oscillator, ω_0, by

$$\omega = \sqrt{\omega_0^2 - \gamma^2}. \tag{3.12}$$

It turns out that this correction is minor, on the order of 1 Hz to 2 Hz.

While it was not the plan initially, a transverse trap frequency measurement in the $R = 0$ configuration can also be used to check the accuracy of our value for w_0, through the relation $w_0 = \sqrt{-4U_0/m\omega_r^2}$. As a consistency check, we perform multiple measurements varying the power. This is shown in figure 3.7. The average result scaled to our standard P/Δ is $\omega_{r,R=0} = 2\pi \times 298(7)\,\mathrm{Hz}$. The self-consistent beam waist from the trap frequency measurement of the $R = 0$ lattice is $w_0 = 115\,\mu\mathrm{m}$. The extrapolated transverse trap frequency of the $R = 0.25$ lattice is $\omega_{r,R=0.25} = 2\pi \times 447\,\mathrm{Hz}$. Concerns that our inability to get these results in the lattice itself may indicate poor overlap of the incoming and retroreflected beams resulting in a strange transverse potential were investigated and ruled out to the accuracy of absorption imaging. We conclude that, unless there exists a perfect intermediate excitation strength that produces a significant oscillation of the atoms without obscuring the nature of the potential they reside in, and assuming that it does the significant effort required to find it is no deterrence,

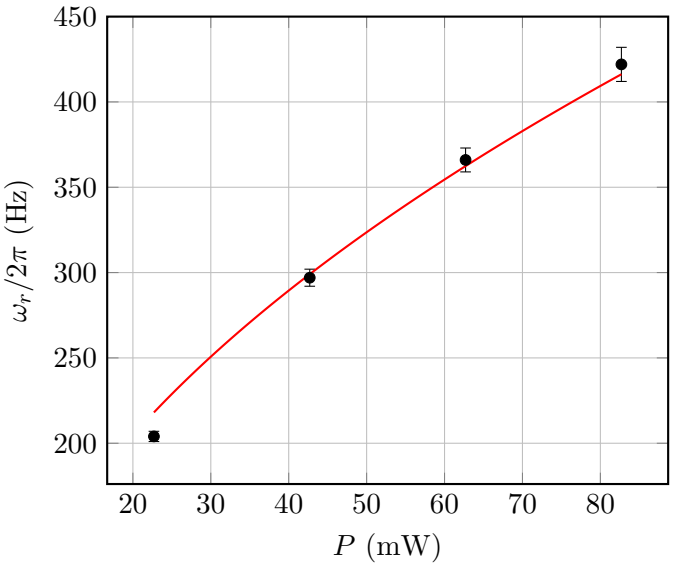

Figure 3.7: For a harmonic trap $\omega_r \propto \sqrt{U_0} \propto \sqrt{P}$. Keeping the detuning constant at $2\pi \times 160\,\mathrm{GHz}$ and varying the power this scaling is verified for the $R = 0$ lattice, increasing confidence in the measurement and the extracted value of w_0.

this type of measurement is not a viable way to directly measure the transverse trap frequency of a partially modulated lattice.

3.4.2 Light Shifts and Thermal Effects

To measure the light shift of the lattice, we proceed as in section 2.4.2. The comparison between the $R = 0$ and $R = 0.25$ lattices is complicated by two issues. Firstly, even at $\Delta = -2\pi \times 160\,\mathrm{GHz}$, for the $R = 0$ lattice, the force enacted upon the atoms by the scattering photons pushes them out of the field of view quite rapidly. This means that it is not possible to select from a range of temperatures to measure the light shift at; the temperature of the atoms is simply 26 µK. This is colder than the atoms ever are in the $R = 0.25$ lattice, which means we need to correct for the light shift due to the potential energy distribution of the atoms at two different temperatures. Secondly, because in the $R = 0.25$ case each lattice trough is only some 400 nm wide (see figure 3.1) we must use the 3D version of f for it. For $R = 0$ we restrict the imaging to the centre of the z axis to work with the 2D version like for the dipole trap. Figure 3.8 shows Δ_f in 2 and 3 dimensions as a function of the temperature of the atoms.

There are two conditions we hope to see the lattice fulfill with these measurements. One is, of course, that the measured light shift is approximately the calculated value. The other is the relation between a lattice and a single-beam potential depth found in section 3.1.1, $V_0 = \left(1 + \sqrt{R}\right)^2 U_0$. That is, we expect $\Delta_{\mathrm{meas},R=0.25} = 2.25\Delta_{\mathrm{meas},R=0}$. The data are shown in figure 3.9. As in section 2.4.2 we measure a calibration error in the position of the resonance without light of $\Delta_0 = 0.280\Gamma$ which we sub-

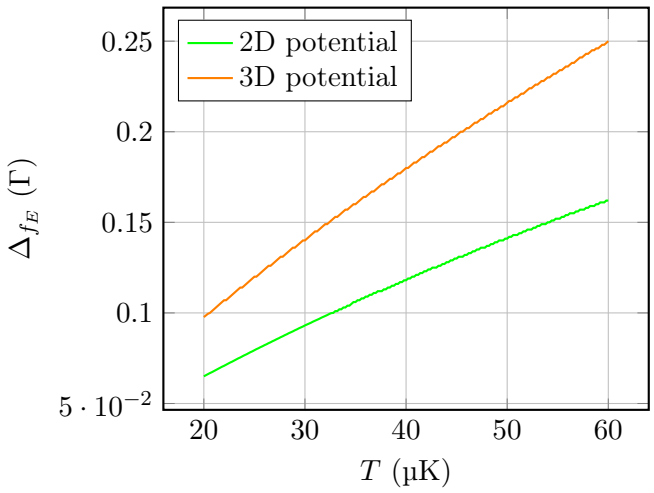

Figure 3.8: This plot is generated by numerically finding the maximum of equation 2.19 for the 2D and 3D versions of f_E and various values of T. The values most of interest are $\Delta_{f_{E,2D}}(26\,\mu K) = -0.082\Gamma$ and $\Delta_{f_{E,3D}}(48\,\mu K) = -0.209\Gamma$.

tract from the presented data for simplicity. The total light shifts are $\Delta_{LS,R=0.25} = \Delta_{meas,R=0.25} + \Delta_{f_{3D}}(48\,\mu K) = -0.708(37)\Gamma$ and $\Delta_{LS,R=0} = \Delta_{meas,R=0} + \Delta_{f_{2D}}(26\,\mu K) = -0.332(22)\Gamma$. The error margins are the combined statistical errors of the Lorentzian fits. In terms of trap depth these values correspond to $T_{d,R=0.25} = -206(11)\,\mu K$ and $T_{d,R=0} = -96.6(64)\,\mu K$. These values are much lower than those the trap frequency measurements predicted, $-274\,\mu K$ and $-122\,\mu K$ respectively. The self consistent beam waist for the $R = 0.25$ lattice is $w_0 = 132\,\mu m$. Although these measurements are in poor agreement with others, they do give a consistent answer to the question of whether the lattice troughs are being loaded with atoms. The ratio of the two values is 2.13, which is within 5 % of the expected 2.25. Regardless of whether the exact results are quantitatively reliable on their own, they were determined in the same manner and thus their ratio lays claim to significance beyond that of the numerical values of its constituents. Atoms are being loaded into the bottoms of the lattice troughs, and appearances to the contrary are explained by their temperature.

3.4.3 Axial Trap Frequency, Parametric Heating

The optical lattice's axial frequency is designed to be around 276 kHz to match the membrane's frequency. This is too fast for an oscillation to be seen with the time resolution of our experimental control, even if we did overcome the spacial problems of seeing small changes in the axial direction of an atomic ensemble longer than the field-of-view. This means, we cannot use the method with which we have been measuring transverse trap frequencies. An alternative is parametric heating. The principle of this technique is to modulate the lattice, either in its intensity or in its position, at various frequencies in an effort to heat atoms out of it. An unusually high number of lost atoms indicates a resonance has been hit, where the strongest signal is expected

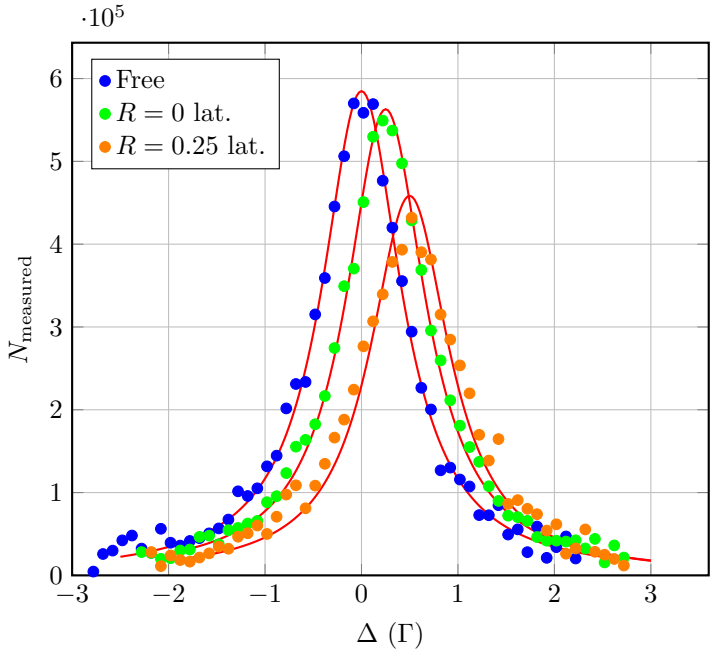

Figure 3.9: The light shift measurement for free atoms, and for atoms confined in either lattice configuration. For convenience the imaging detuning is given in units of the natural linewidth, $\Gamma = 2\pi \times 6.065\,\text{MHz}$. In the $R = 0.25$ lattice the light shift is $\Delta_{\text{meas},R=0.25} = -0.779\Gamma$ and in the $R = 0$ lattice it is $\Delta_{\text{meas},R=0} = -0.530\Gamma$.

for $\omega_{\text{mod}} = 2\omega_z$.

The parametric harmonic oscillator is a problem known and studied in the framework of classical mechanics. The resonance at $\omega_{\text{mod}} = 2\omega_z$ can be found by considering an equation of motion of the form

$$\ddot{x} + \omega_z^2 \left(1 + h\cos\left(\left(2\omega_z + \epsilon\right)t\right)\right) x = 0, \tag{3.13}$$

where both h and ϵ are small. It is found, that sufficiently close to resonance the amplitude of oscillations grows exponentially. Further resonances occur at freqencies $\omega_{\text{mod}} = 2\omega_z/n$, with n integral, but their width decreases with h^n, requiring more and more exact driving to be observed [64].

A quantum mechanical description of parametric heating in a harmonic oscillator qualitatively agrees with the classical case, including the scaling of the widths of the resonances [65]. The problem has been extended to fully modulated 1D optical lattices. The main modification is a redshift in the resonances in comparison to the harmonic case. Additionally, a resonance is found to occur at $\omega_{\text{mod}} = 4\omega_z$ [66].

To implement parametric excitation in our lattice, we add a sinusoidal modulation from a function generator[3] onto the feedback signal of our intensity stabilisation controlling the AOM. The intensity stabilisation is fully compatible with this use because

[3] DS345 by SRS

the modulation is much faster than its response time. Our electronic setup is such, that this modulation is attenuated by an amount depending on its frequency. This must be compensated, for as the width of the resonances scale with the modulation amplitude, so it is desirable for it to be constant. For this reason, the modulation is calibrated over the full range of frequencies scanned by measuring the lattice intensity variation with a photo diode and oscilloscope. The amplitude of the modulation on the function generator can then be adjusted so that the modulation on the light is a constant fraction of the total amplitude. In this manner the real modulation amplitude on the light can be set to a constant 10 %.

Hoping to see resonances at ω_z, $2\omega_z$, and $4\omega_z$, images where the lattice was modulated were taken alternately with images where the lattice was just held for the same amount of time, and the modulation frequency was scanned from 0.1 MHz to 1 MHz in 20 kHz steps. No significant signals could be detected in comparative atom loss for any modulation frequency. As an alternative, we measured transverse temperature, anticipating that the lattice would mix the motional degrees of freedom sufficiently fast that a temperature change could be observed. This too was unsuccessful. The data for different modulation frequencies were scattered randomly about the expected temperature of 42 µK without any apparent patterns.

There was however a highly noticeable signal in another quantity. When modulated, the centre of the atom cloud would be significantly displaced from the unmodulated case. Displacements up to 3 mm were seen, corresponding to over 200 pixels on the camera. The strength of the signal alone called for taking a closer look at this effect.

As was briefly discussed in section 3.1, partially modulated lattices have a region in their potential with some radial confinement but without significant axial confinement. This region, the faster decline of axial confinement with the energy of an atom, and the stronger anharmonicity in comparison to fully modulated lattices leads to the failure of parametric heating to fully expel atoms from the lattice. Parametric heating does however heat the atoms out of their strong axial confinement. Then, the imbalance in the intensity of incident and reflected beams leads to a preferred direction for the average force on the atoms, and thus to a displacement of the atom cloud. This behaviour could be confirmed qualitatively with a classical Monte Carlo simulation.

The data for four different sets of lattice parameters are collected in figure 3.10. The shift of the atom cloud centre, δx_c, is normalised to 1 in each data set, after which they are offset for visibility. Each scan shows each of the expected resonances around ω_z, $2\omega_z$, and $4\omega_z$ respectively, with a significant but not unreasonable red shift from the values calculated in the harmonic case. Further, the scaling of these frequencies with P/Δ is verified with one set of data taken at half the usual value, resulting in a reduction in trap frequencies of about a factor $\sqrt{2}$. The average value extracted from just the resonances at $2\omega_z$, which have the best visibility, is $\omega_z = 2\pi \times 264\,\mathrm{kHz}$, which is near the predicted value of $2\pi \times 277\,\mathrm{kHz}$. Averaging instead over all peaks yields $\omega_z = 2\pi \times 245\,\mathrm{kHz}$, revealing a stronger measured red shift in the ω and 4ω resonances.

The peaks of the resonances become flatter as less power is used. At least in part this is an artefact of how well we can modulate the lattice. The model shows that stronger, sharper resonances are produced for smaller modulation amplitudes, as long

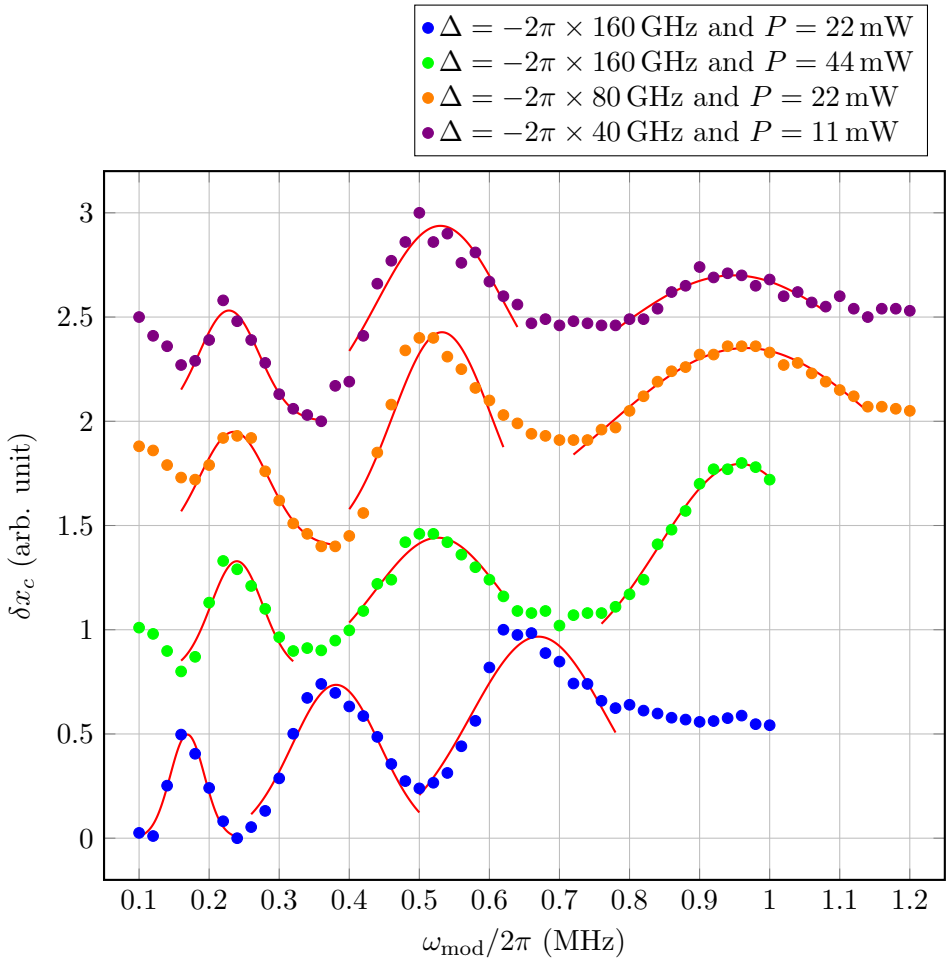

Figure 3.10: The parametric heating resonances produce a signal in the centre position of the atom cloud. The resonances are fit quite nicely with Gaussian peaks, although some asymmetries are present in the data. The widths of the peaks scale well with the modulation frequency but do not reproduce the derived scaling laws (i.e. a power series in h).

as a small threshold is exceeded. Here we are limited by the minimum output and step size of the function generator for the lower modulation frequencies, and when in doubt opted for a constant modulation amplitude rather than a small modulation amplitude. For this reason, the amplitude in the data set for a lattice power of 11 mW is modulated at around 18 %.

The other reason for the lower quality of the resonance at lower lattice power is the lattice lifetime, $\tau(P = 11\,\mathrm{mW}) = 76\,\mathrm{ms}$. This means, that there is less time to modulate the lattice before a measurement must be made to still see enough atoms. The signal is further reduced by the exact mechanism of the atoms moving along the lattice. If an atom is heated sufficiently far out of its lattice site to move along the

lattice, then it is likely to travel quite far axially. This leads to a large spread of the moved atoms, and diffuse clouds give a weaker signal.

In conclusion, figure 3.10 shows a cleaner spectrum with sharper peaks than ever recorded for this lattice in previous iterations of the setup. It thus lends us confidence in the calibration of our atomic frequency when tuning it to perform experiments with the membrane. The wrinkle represented by the unexpected cooling without obvious evaporation during loading is interesting, and if studied more closely the involved thermodynamics may guide the implementation of the transfer process between traps in future. Nevertheless, the converging lines of evidence represented by these measurements, the temperature measurements, and the ratio of the single-beam and lattice light shift measurements, as well as the reasonable explanation we can provide for the strange result of the transverse frequency measurement lead us to believe that the lattice behaves as we expect.

Chapter 4

Outlook: Coupling Experiments

The ultimate goal of the work presented in this thesis was improving and characterising the setup of our atom-light interface to be used in coupling experiments. For this reason, this closing chapter takes a step back from the slew of technical details presented so far, to give a brief and broad overview of what comes next. Section 4.1 discusses the atom-membrane experiment, and contains the results of a first experiment coupling the new atomic ensemble to the membrane. Then, section 4.2 sketches the current state of plans to store single photons from a semiconductor quantum dot with this atomic ensemble.

4.1 Atom-Membrane Coupling

The membrane side of the atom-membrane coupling experiment consists of a stoichiometric silicon nitride membrane.[1] This membrane is mounted in a cavity in a membrane-in-the-middle configuration. The assembly process of this system is detailed in [67]. We currently use a copy of the original. There are some minor differences between the two that are pointed out in [18]. The membrane is square in shape with side length l and can oscillate out of plane like a square drum, i.e. with the frequency of a mode i, j given by [68]

$$\omega_{i,j} = \frac{\pi}{l}\sqrt{\frac{S}{\rho}\,(i^2 + j^2)}. \tag{4.1}$$

The definitions and values of the parameters of this equation are listed along with other interesting properties of the membrane and the cavity in table 4.1. The cavity is evacuated to a pressure of about 10^{-7} mbar. This is sufficiently low not to limit the Q-factor of the membrane, which saturates at 1.8×10^6.

The motion of the membrane is read out with a detection beam. The cavity resonance frequency is modified through the membrane's motion, which induces a phase shift in the reflected detection beam. This phase shift is measured with a balanced homodyne detection system, described in [18], with the small difference that the laser

[1] These are made by and purchased from Norcada

Symbol	Meaning	Value
l	Side length	1.5 mm
S	Tensile stress	930 MPa
ρ	Mass density	2700 kg m^{-3}
d	Thickness	39.1 nm
M	Effective mass	117 ng
r_m	Amplitude reflectivity	0.404
ω_m	Frequency	$2\pi \times 276.3$ kHz
Γ_m	Damping rate	0.96 Hz
Q	Quality factor	1.8×10^6
$\mathcal{F}$	Cavity finesse	700

Table 4.1: This table listing membrane properties is adapted from [18]. The frequency, mass, damping rate, and quality factor all refer to the fundamental membrane mode.

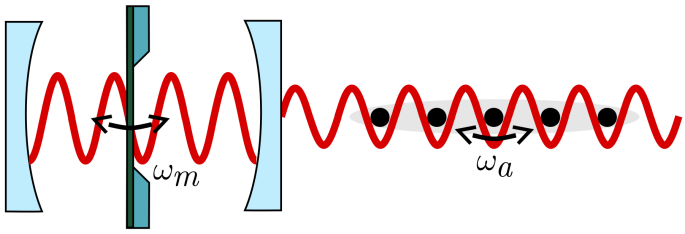

Figure 4.1: This drawing shows the membrane in the middle of an optical cavity, oscillating at a frequency ω_m, coupled to far away ultracold atoms via an optical lattice. The atoms in turn oscillate at a frequency ω_a in the lattice.

source has also been changed to the titanium sapphire laser that generates the lattice. The voltage signal from the photo diode is sent to a spectrum analyser. The spectrum analyser outputs the power spectral density of this voltage, which is proportional to the power spectral density of the membrane displacement. Measuring the power spectrum over time allows us to determine the damping rate of the membrane directly, without needing to calibrate the data against a known temperature.

4.1.1 Theoretical Overview

The basic setup of a membrane coupled to atoms in an optical lattice is shown in figure 4.1. The interaction Hamiltonian for this system is [52]

$$\hat{\mathcal{H}} = \hbar g \left(\hat{b}_m + \hat{b}_m^\dagger\right)\left(\hat{b}_a + \hat{b}_a^\dagger\right). \tag{4.2}$$

Here $\hat{b}_m$ and $\hat{b}_a$ are bosonic annihilation operators for the membrane and atomic modes respectively and g_N is a coupling constant given by

$$g = |r_m|\omega_a \sqrt{\frac{Nm\omega_a}{M\omega_m}} \frac{2\mathcal{F}}{\pi}, \tag{4.3}$$

where ω_a is the oscillation frequency of the atoms in the lattice previously called $\omega_{\mathrm{lat},z}$, and other parameters are defined in table 4.1. This Hamiltonian is one way to derive a set of coupled equations of motion for the atom and membrane displacements. These equations are easily decoupled in frequency space, after which the sympathetic damping rate can in turn be derived [18]. In this model the result is

$$\Gamma_{\mathrm{sym}} = \frac{\eta^2 t^2 g^2 \Gamma_a}{(\omega_a - \omega_m)^2 + \Gamma_a^2/4}, \tag{4.4}$$

where η is the cavity incoupling efficiency, t is the single pass amplitude transmission between atoms and membrane, and Γ_a is the atomic damping rate. The relation between η, t, and R as used in chapter 3 is $R = \eta^2 t^4 \approx t^4 \approx 0.25$. The atomic damping rate, Γ_a, is the sum of any forced damping as through laser cooling, which is off for the upcoming results, and the intrinsic damping rate from light-induced momentum diffusion. The latter is related to the photon scattering rate by the Lamb-Dicke parameter [31]

$$\Gamma_{a,D} = \eta^2 \Gamma_{\mathrm{scat}} = \frac{\omega_{\mathrm{recoil}}}{\omega_a} \Gamma_{\mathrm{scat}} = k^2 x_{\mathrm{zpf}}^2 \frac{\Gamma V_0}{\hbar \Delta}, \tag{4.5}$$

where $x_{\mathrm{zpf}}^2 = \hbar/2m\omega_a$ is the zero point amplitude of a single atom.

An important result of [18] is that this picture is too simple to accurately predict or explain observed self-oscillations in the atom-membrane hybrid system. In a more complete picture the coupling between atoms and the membrane is delayed by τ. This is found to be partially explained by the time taken for light to propagate between the atoms and the membrane. Additionally, when the lattice is nearly resonant with the atomic transition, the back-action of the atoms onto the light gives rise to an effective delay. The model outlined above can be modified to account for a delay in the coupling analytically, but the resulting expressions are a little unwieldy.

4.1.2 First Results

A sympathetic cooling experiment was performed with the atomic ensemble loaded into the lattice from the dipole trap. The data are shown in figure 4.2. The measured damping rate is the sum of all the damping rates, $\Gamma_{\mathrm{tot}} = \Gamma_{\mathrm{sym}} + \Gamma_{\mathrm{opt}} + \Gamma_m$. The sum of the optomechanical damping rate Γ_{opt} and the intrinsic damping rate Γ_m is found by performing a measurement with identical laser parameters but without atoms. The sympathetic cooling rate is then found by subtracting the result of this second measurement, from the total measured damping rate.

The full, delay-coupled theory predicts a much sharper, stronger onset of cooling once $\omega_{z,\mathrm{lat}} \geq \omega_m$, quite a narrow resonance, and a small region just to the red of

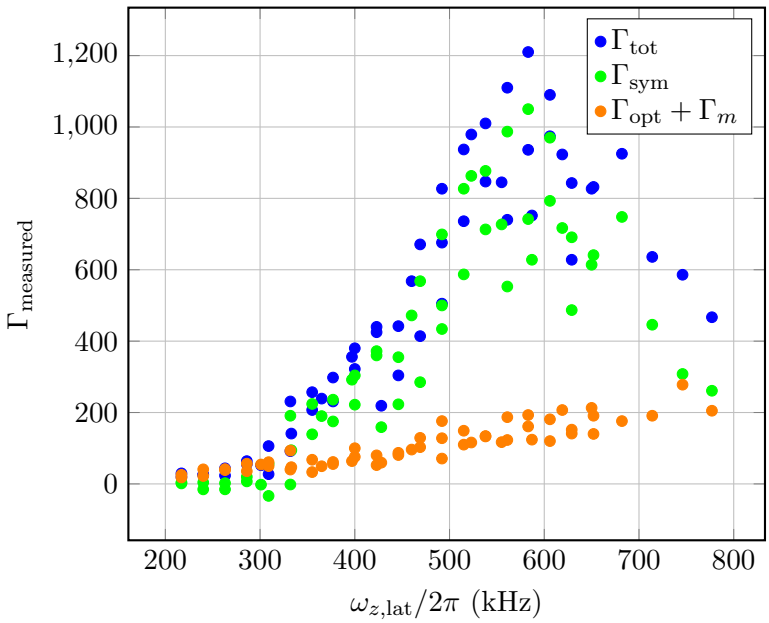

Figure 4.2: Data from the spectrum analyser in the first sympathetic cooling experiment wherein the lattice is loaded from the dipole trap. The lattice detuning is $\Delta = -2\pi \times 5\,\text{GHz}$. The optomechanical and intrinsic damping rate, Γ_{opt} and Γ_m, are subtracted from the total damping rate, Γ_{tot}, to yield the sympathetic cooling rate, Γ_{sym}. The peak of the resonance is around 600 kHz.

the resonance where Γ_{sym} turns negative. The displacement and broadening both indicate that the atoms are not loaded into the lattice deeply and adiabatically for the experiment parameters. As was discussed in section 3.2.1, the usable powers are limited by noise peaks. In this experiment this maximum was just under 20 mW. No significant change in the damping rate was seen by scanning through the possible powers for $\Delta = -2\pi \times 40\,\text{GHz}$. Thus, the detuning was reduced to $\Delta = -2\pi \times 5\,\text{GHz}$. Due to the minimum power we can set to get a spike free ramp, this means the lattice is effectively switched on suddenly and in its entirety for low set values of the lattice power. Absorption imaging confirms that the shallower lattices generated by low powers at this detuning are hardly loaded with atoms. Temperature measurements show that the atom temperature after the transfer procedure rises linearly with lattice power; at the parameters where the resonance in Γ_{sym} is seen the atoms are easily over 100 µK warm.

These problems need to be addressed in order to reap the benefits of the dipole trap. Improvements to the transfer process will be easier to work towards and implement now that the boundary conditions of the lattice to be optimised are understood. The fact that the usable power is not limited by the fundamental optimum but by another technical problem is unfortunate, and probably could be addressed with electrical filtering in the current setup. This would also allow working at a higher lattice detuning, which suppresses the effective atomic back-action delay that can limit sym-

pathetic cooling [18]. This issue will likely be resolved in the new membrane-cavity setup currently being built as we are aware of the problem ahead of time.

4.1.3 Cryogenics, Phononic Crystal Membranes, and Internal State Coupling

In the classical limit, the final temperature of the sympathetically cooled membrane is proportional to the temperature of its environment,

$$T_{\mathrm{sym}} = T_{\mathrm{bath}} \frac{\Gamma_m}{\Gamma_m + \Gamma_{\mathrm{opt}} + \Gamma_{\mathrm{sym}}}. \tag{4.6}$$

For this reason, pre-cooling the membrane with a cryostat brings us that much closer to the quantum regime. As the temperature is a stand in for the phonon occupation number of the membrane's vibrational mode, at time of writing we are investigating and comparing the vibrational isolation achievable for the membrane in closed-cycle cryostats and in helium flow cryostats, with the goal of starting the sympathetic cooling process on a 4 K cold membrane in future.

To isolate membranes from their support structure they can be embedded in a phononic crystal [69]. In our lab, we have such phononic crystal membranes, which were developed in collaboration with the group of C. Regal. While the Q-factor appears unchanged from the membranes without phononic crystals we have observed a lower noise floor on the spectrum of such an embedded membrane. We intend our next membrane setup to combine a phononic crystal membrane cavity with cryogenics.

We are also testing novel membrane structures called tether membranes [70]. Unlike our current square membranes that are attached to their frames all about the perimeter, tether membranes are only connected to their frames via four narrow strips of material connecting the corners of the frame and the resonator. These "trampolines" have a much smaller mass than their drum-like counterparts, a mere 2 ng being typical. Their tethers also serve to minimise interaction with the environment, reaching Q-factors of the fundamental mode around 1.5×10^7. Further, it is possible to combine these membranes with photonic crystal structures to achieve a very high reflectivity. As promising as all these properties are, cavities built with current tether membranes have optical modes far from TEM_{00}, which would drastically reduce the coupling efficiency and negate the advantages in our hybrid system, and indicates that another round of fine-tuning the membrane parameters is required before we can use them.

Finally, we are looking into a coupling scheme between the internal states of the atomic ensemble and the membrane's motion as described in [71]. The advantages are plentiful. The level of control over the electronic atomic states is excellent. The frequency on the atomic side would no longer be limited to the possible frequencies of the optical lattice, allowing resonant coupling to more types of resonators and more modes. Further, the internal states of atoms can be used to implement proposals for entanglement or even quantum noise free trajectories that require effective negative mass oscillators [72, 73].

4.2 Quantum Memory

Semiconductor quantum dots generally are excellent sources of single photons, due to their high brightness and narrow linewidths [74]. The most commonly studied structures, self-assembled InGaAs quantum dots, emit around 950 nm. It was not until a few years ago that tuning the frequency of a quantum dot to match the D_1 or D_2 lines of a rubidium vapour was demonstrated [75]. The same group that originally studied "artificial rubidum" then slowed single photons emitted by this quantum dot with a rubidium vapour cell, using the double absorption resonance technique to store the spectrally broad light [76].

The single photon source of our experiments is described in [11]. An experiment to store these single photons with a hot rubidium vapour cell is currently being set up. First trials have successfully delayed classical light via electromagnetically induced transparency. The high optical depth of the atom cloud confined in the dipole trap could combine the efficiency advantage of high OD commonly found only in vapour cells with the coherent control advantages of cold atoms. Specifically, a direct comparison of storing photons with a vapour cell and with a cold atomic ensemble will be possible with the setup developed in this thesis.

Appendix A

Tables of Trap Parameters

Parameter	Symbol	Conditions	Value
Wavelength	λ_{dip} or λ	Spec.	1064 nm
Output power	P_{out}	Meas. and spec.	42 W
Power at atoms	P	Meas. (after chamber)	21 W
Beam waist	w_0		
-at AOM		Meas. (beam profiling)	550 µm
-at atoms		Meas. (beam profiling)	92 µm
		ω_r meas.	85 µm
		T_d meas.	82 µm
Rayleigh range	z_R	ω_r meas.	213 mm
Atom number	N_{at}	Meas. (abs. img. 100 ms)	$\geq 2.4 \times 10^7$
		Meas. (abs. img. 2 s)	$\geq 1.6 \times 10^7$
		Meas. (abs. img. 4 s)	$\geq 1.3 \times 10^7$
Lifetime	τ		
-Evaporative	τ_{evap}	Meas. (abs. img. fit)	1.1 s
-Collisional	τ_{bg}	Meas. (abs. img. fit)	12.4 s
Final temperature	T_f	Meas. (TOF fit)	34 µK
Temperature	T_{at}	Meas. (TOF 100 ms)	54 µK
		Meas. (TOF 2 s)	42 µK
Trap frequency			
-Axial	$\omega_{z,\text{dip}}$	ω_r meas.	$2\pi \times 1.7$ Hz
-Transverse	$\omega_{r,\text{dip}}$	Meas. (breathing mode)	$2\pi \times 611$ Hz
	or ω_r	T_d meas.	$2\pi \times 657$ Hz
		w_0 meas.	$2\pi \times 525$ Hz

continued on next page

continued from previous page

Parameter	Symbol	Conditions	Value
Trap depth	T_d or	Meas. (light shift)	$-300\,\mu K$
	$U_0 = k_B T_d$	ω_r meas.	$-280\,\mu K$
		w_0 meas.	$-240\,\mu K$
RMS $(1/e)$ width			
-Axial	σ_z	ω_r meas. and $T_{at} = 54\,\mu K$	6.6 mm
		ω_r meas. and $T_{at} = 34\,\mu K$	5.2 mm
-Transverse	σ_r	ω_r meas. and $T_{at} = 54\,\mu K$	18.6 µm
		ω_r meas. and $T_{at} = 34\,\mu K$	14.8 µm
		Meas. (TOF fit)	21(10) µm
Aspect ratio	A	ω_r meas.	355
Optical depth	OD or	Meas. (abs. img. 100 ms)	≥ 1400
	$OD_{p,r}$	ω_r meas., $T_{at} = 54\,\mu K$, and	
		$N_{at} = 2.4 \times 10^7$	2136

Table A.1: Collected measurements of the dipole trap. In the condition column "spec." means the value is specified by the laser manufacturer, whereas "meas. (*method*)" means a value was measured with the specified method. In particular, times in the brackets are hold times of the dipole trap. Finally, a note in the form "x meas. and y" means the value is calculated from the measured value of x assuming y.

Parameter	Symbol	Conditions	Value
Detuning from D2	Δ	Meas. (wave meter)	$-2\pi\times40$ GHz
Incident power	P	Meas. (before chamber)	11 mW
Int. ref. coeff.	R	Meas. (after isolator)	0.25 to 0.27
Beam waist	w_0	Meas. (beam profiling)	100 µm
		$\omega_{r,R=0}$ meas.	115 µm
		$T_{d,R=0.25}$ meas.	132 µm
Trap frequency			
-Axial	$\omega_{z,\mathrm{lat}}$	Meas. (parametic heating)	$2\pi\times262$ kHz
	or ω_z	$\omega_{r,R=0}$ meas.	$2\pi\times277$ kHz
		w_0 meas.	$2\pi\times317$ kHz
-Transverse	$\omega_{r,R=0.25}$	$\omega_{r,R=0}$ meas.	$2\pi\times447$ Hz
	or ω_r	w_0 meas.	$2\pi\times591$ Hz
Trap depth	T_d or	Meas. (light shift)	-206 µK
	$V_0 = k_B T_d$	ω_r meas.	-274 µK
		w_0 meas.	-360 µK
Atom number	N_{at}	Meas. (abs. img. 10 ms)	$\geq 2.4\times10^7$
		Meas. (abs. img. 70 ms)	$\geq 1\times10^7$
Lifetime	τ	Meas. (abs. img. fit)	76 ms
Temperature	T_{at}	Meas. (TOF 10 ms)	35 µK
		Meas. (TOF 70 ms)	41 µK
Heating rate	$\dot{T}$	Meas. (TOF fit)	0.083 µK ms^{-1}

Table A.2: Collected measurements of the optical lattice at $\Delta = -2\pi\times40$ GHz. The meanings of the terms in the conditions column are explained in table A.1.

Parameter	Symbol	Conditions	Value
Detuning from D2	Δ	Meas. (wave meter)	$-2\pi\times160$ GHz
Incident power	P	Meas. (before chamber)	44 mW
Lifetime	τ	Meas. (abs. img. fit)	270 ms
Temperature	T_{at}	Meas. (TOF 10 ms)	33 µK
		Meas. (TOF 200 ms)	50 µK
Heating rate	$\dot{T}$	Meas. (TOF fit)	0.055 µK ms^{-1}

Table A.3: Additional measurements of the optical lattice at $\Delta = -2\pi\times160$ GHz. Measurements conducted for both sets of detuning and power that yield the same values are not listed again here. The meaning of the terms in the conditions column is explained above.

List of Figures

List of Tables

Bibliography

[1] J. I. Cirac and P. Zoller, *Quantum computations with cold trapped ions*, Phys. Rev. Lett. **74**, 4091 (1995).

[2] B. B. Blinov, D. Leibfried, C. Monroe, and D. J. Wineland, *Quantum computing with trapped ion hyperfine qubits*, Quantum Inf. Process. **3**, 45 (2004).

[3] D. Jaksch, J. I. Cirac, P. Zoller, S. L. Rolston, R. Côté, and M. D. Lukin, *Fast quantum gates for neutral atoms*, Phys. Rev. Lett. **85**, 2208 (2000).

[4] I. H. Deutsch, G. K. Brennen, and P. S. Jessen, *Quantum computing with neutral atoms in an optical lattice*, in *Scalable Quantum Computers*, pp. 155–173 (Wiley-Blackwell) (2005).

[5] L.-M. Duan, M. D. Lukin, J. I. Cirac, and P. Zoller, *Long-distance quantum communication with atomic ensembles and linear optics*, Nature **414**, 413 (2001).

[6] K. Stannigel, P. Rabl, A. S. Sørensen, P. Zoller, and M. D. Lukin, *Optomechanical transducers for long-distance quantum communication*, Phys. Rev. Lett. **105** (2010).

[7] D. P. Divincenzo, *The physical implementation of quantum computation*, in *Scalable Quantum Computers*, pp. 1–13 (Wiley-Blackwell) (2005).

[8] K. Hammerer, A. S. Sørensen, and E. S. Polzik, *Quantum interface between light and atomic ensembles*, Rev. Mod. Phys. **82**, 1041 (2010).

[9] S. L. Braunstein and A. K. Pati (editors), *Quantum Information with Continous Variables* (Kluwer Academic Publishers) (2001).

[10] M. T. Rakher, R. J. Warburton, and P. Treutlein, *Prospects for storage and retrieval of a quantum-dot single photon in an ultracold ^{87}Rb ensemble*, Phys. Rev. A **88** (2013).

[11] J.-P. Jahn, M. Munsch, L. Béguin, A. V. Kuhlmann, M. Renggli, Y. Huo, F. Ding, R. Trotta, M. Reindl, O. G. Schmidt, A. Rastelli, P. Treutlein, and R. J. Warburton, *An artificial Rb atom in a semiconductor with lifetime-limited linewidth*, Phys. Rev. B **92** (2015).

[12] Y.-H. Chen, M.-J. Lee, I.-C. Wang, S. Du, Y.-F. Chen, Y.-C. Chen, and I. A. Yu, *Coherent optical memory with high storage efficiency and large fractional delay*, Phys. Rev. Lett. **110** (2013).

[13] M. Aspelmeyer, T. J. Kippenberg, and F. Marquardt (editors), *Cavity Optomechanics*, , Quantum Science and Technology (Springer Science + Business Media) (2014).

[14] K. Hammerer, K. Stannigel, C. Genes, P. Zoller, P. Treutlein, S. Camerer, D. Hunger, and T. W. Hänsch, *Optical lattices with micromechanical mirrors*, Phys. Rev. A **82** (2010).

[15] D. Hunger, S. Camerer, M. Korppi, A. Jöckel, T. Hänsch, and P. Treutlein, *Coupling ultracold atoms to mechanical oscillators*, C. R. Phys. **12**, 871 (2011).

[16] A. Jöckel, A. Faber, T. Kampschulte, M. Korppi, M. T. Rakher, and P. Treutlein, *Sympathetic cooling of a membrane oscillator in a hybrid mechanical–atomic system*, Nat. Nanotechnol. **10**, 55 (2014).

[17] T. A. Palomaki, J. W. Harlow, J. D. Teufel, R. W. Simmonds, and K. W. Lehnert, *Coherent state transfer between itinerant microwave fields and a mechanical oscillator*, Nature **495**, 210 (2013).

[18] A. Faber, *Sympathetic cooling and self-oscillations in a hybrid atom-membrane system*, Ph.D. thesis, Universität Basel (2016).

[19] A. V. Gorshkov, A. André, M. D. Lukin, and A. S. Sørensen, *Photon storage in Λ-type optically dense atomic media. II. Free-space model*, Phys. Rev. A **76**, 033805 (2007).

[20] B. M. Sparkes, J. Bernu, M. Hosseini, J. Geng, Q. Glorieux, P. A. Altin, P. K. Lam, N. P. Robins, and B. C. Buchler, *An ultra-high optical depth cold atomic ensemble for quantum memories*, J. Phys. Conf. Ser. **467**, 012009 (2013).

[21] S. J. M. Kuppens, K. L. Corwin, K. W. Miller, T. E. Chupp, and C. E. Wieman, *Loading an optical dipole trap*, Phys. Rev. A **62** (2000).

[22] R. Grimm, M. Weidemüller, and Y. B. Ovchinnikov, *Optical dipole traps for neutral atoms*, Adv. At., Mol., Opt. Phys. **42**, 95 (2000).

[23] A. Jöckel, *Sympathetic cooling of a membrane oscillator in a hybrid mechanical-atomic system*, Ph.D. thesis, Universität Basel (2014).

[24] H. J. Metcalf and P. van der Straten, *Laser Cooling and Trapping*, , Graduate Texts in Contemporary Physics (Springer New York) (1999).

[25] A. Franzen, *ComponentLibrary*, Licenced under CC BY-NC 3.0 (2006).

[26] W. Ketterle, D. S. Durfee, and D. M. Stamper-Kurn, *Making, probing and understanding Bose-Einstein condensates*, Proceedings of the International School of Physics "Enrico Fermi" **140**, 67 (1999).

[27] G. Reinaudi, T. Lahaye, Z. Wang, and D. Guéry-Odelin, *Strong saturation absorption imaging of dense clouds of ultracold atoms*, Opt. Lett. **32**, 3143 (2007).

[28] D. A. Steck, *Rubidium 87 D line data*, Online, revision 2.1.5 (2015).

[29] L. Allen and J. H. Eberly, *Optical Resonance and Two-Level Atoms*, *Monographs and Texts in Physics and Astronomy*, volume XXVIII (John Wiley & Sons, Inc., New York), 1st edition (1975).

[30] C. Cohen-Tannoudji, *Atomic motion in laser light*, in J. Dalibard, J. M. Raimond, and J. Zinn-Justin (editors), *Fundamental Systems in Quantum Optics*, Les Houches, Session LIII, 1990 (Elsevier BV) (1992).

[31] S. Stenholm, *The semiclassical theory of laser cooling*, Rev. Mod. Phys. **58**, 699 (1986).

[32] A. Corney, *Atomic and Laser Spectroscopy* (Oxford University Press) (1977).

[33] R. Loudon, *The Quantum Theory of Light* (Oxford University Press), 3rd edition (2000).

[34] Y. Wang and I. Khoo, *On the Wigner-Weisskopf approximation in quantum optics*, Opt. Commun. **11**, 323 (1974).

[35] M. S. Safronova and U. I. Safronova, *Critically evaluated theoretical energies, lifetimes, hyperfine constants, and multipole polarizabilities in* ^{87}Rb, Phys. Rev. A **83** (2011).

[36] A. Kramida, Y. Ralchenko, J. Reader, and the NIST ASD team, *NIST Atomic Spectra Database (version 5.3)* (2015).

[37] M. Kubasik, *Towards Spin Squeezing in Cold Atomic Ensembles*, Ph.D. thesis, The Institute of Photonic Sciences (2009).

[38] W. Alt, *Optical control of single neutral atoms*, Ph.D. thesis, Rheinische Friedrich-Wilhelms-Universität Bonn (2004).

[39] H. Katori, M. Takamoto, V. G. Pal'chikov, and V. D. Ovsiannikov, *Ultrastable optical clock with neutral atoms in an engineered light shift trap*, Phys. Rev. Lett. **91** (2003).

[40] C. D. Herold, V. D. Vaidya, X. Li, S. L. Rolston, J. V. Porto, and M. S. Safronova, *Precision measurement of transition matrix elements via light shift cancellation*, Phys. Rev. Lett. **109** (2012).

[41] J. H. Müller, P. Petrov, D. Oblak, C. L. G. Alzar, S. R. de Echaniz, and E. S. Polzik, *Diffraction effects on light–atomic-ensemble quantum interface*, Phys. Rev. A **71** (2005).

[42] M. Kubasik, M. Koschorreck, M. Napolitano, S. R. de Echaniz, H. Crepaz, J. Eschner, E. S. Polzik, and M. W. Mitchell, *Polarization-based light-atom quantum interface with an all-optical trap*, Phys. Rev. A **79** (2009).

[43] Crystal Technologies, Inc., *Acousto-Optic application note – modulator model 3000 series* (2006).

[44] L. You and M. Holland, *Ballistic expansion of trapped thermal atoms*, Phys. Rev. A **53**, R1 (1996).

[45] O. J. Luiten, M. W. Reynolds, and J. T. M. Walraven, *Kinetic theory of the evaporative cooling of a trapped gas*, Phys. Rev. A **53**, 381 (1996).

[46] W. Ketterle and N. V. Druten, *Evaporative cooling of trapped atoms*, Adv. At., Mol., Opt. Phys. **37**, 181 (1996).

[47] A. J. Olson, R. J. Niffenegger, and Y. P. Chen, *Optimizing the efficiency of evaporative cooling in optical dipole traps*, Phys. Rev. A **87** (2013).

[48] J.-F. Clément, J.-P. Brantut, M. R. de Saint-Vincent, R. A. Nyman, A. Aspect, T. Bourdel, and P. Bouyer, *All-optical runaway evaporation to Bose-Einstein condensation*, Phys. Rev. A **79** (2009).

[49] K. M. O'Hara, M. E. Gehm, S. R. Granade, and J. E. Thomas, *Scaling laws for evaporative cooling in time-dependent optical traps*, Phys. Rev. A **64** (2001).

[50] E. W. Streed, A. P. Chikkatur, T. L. Gustavson, M. Boyd, Y. Torii, D. Schneble, G. K. Campbell, D. E. Pritchard, and W. Ketterle, *Large atom number Bose-Einstein condensate machines*, Rev. Sci. Instrum. **77**, 023106 (2006).

[51] C. Ockeloen, *Quantum Metrology with a Scanning Probe Atom Interferometer*, Ph.D. thesis, Universität Basel (2014).

[52] B. Vogell, K. Stannigel, P. Zoller, K. Hammerer, M. T. Rakher, M. Korppi, A. Jöckel, and P. Treutlein, *Cavity-enhanced long-distance coupling of an atomic ensemble to a micromechanical membrane*, Phys. Rev. A **87** (2013).

[53] F. Kaminski, N. S. Kampel, M. P. H. Steenstrup, A. Griesmaier, E. S. Polzik, and J. H. Müller, *In-situ dual-port polarization contrast imaging of Faraday rotation in a high optical depth ultracold ^{87}Rb atomic ensemble*, Eur. Phys. J. D **66** (2012).

[54] C. Cohen-Tannoudji, J. Dupont-Roc, and G. Grynberg, *Atom-Photon Interactions* (Wiley-VCH) (1998).

[55] C.-Y. Shih and M. S. Chapman, *Nondestructive light-shift measurements of single atoms in optical dipole traps*, Phys. Rev. A **87** (2013).

[56] L. E. Reichl, *A Modern Course in Statistical Physics* (J. Wiley and Sons, New York), 3rd edition (2009).

[57] J. P. Gordon and A. Ashkin, *Motion of atoms in a radiation trap*, Phys. Rev. A **21**, 1606 (1980).

[58] J. Dalibard and C. Cohen-Tannoudji, *Dressed-atom approach to atomic motion in laser light: the dipole force revisited*, J. Opt. Soc. Am. B **2**, 1707 (1985).

[59] T. A. Savard, K. M. O'Hara, and J. E. Thomas, *Laser-noise-induced heating in far-off resonance optical traps*, Phys. Rev. A **56**, R1095 (1997).

[60] M. E. Gehm, K. M. O'Hara, T. A. Savard, and J. E. Thomas, *Dynamics of noise-induced heating in atom traps*, Phys. Rev. A **58**, 3914 (1998).

[61] C. W. Gardiner, J. Ye, H. C. Nagerl, and H. J. Kimble, *Evaluation of heating effects on atoms trapped in an optical trap*, Phys. Rev. A **61** (2000).

[62] M. Korppi, *Optomechanical Coupling between Ultracold Atoms and a Membrane Oscillator*, Ph.D. thesis, Universität Basel (2014).

[63] P. B. Blakie and J. V. Porto, *Adiabatic loading of bosons into optical lattices*, Phys. Rev. A **69** (2004).

[64] L. D. Landau and E. M. Lifshitz, *Mechanics*, *Course of Theoretical Physics*, volume 1 (Butterworth-Heinemann), 3rd edition (1993).

[65] R. Jáuregui, *Nonperturbative and perturbative treatments of parametric heating in atom traps*, Phys. Rev. A **64** (2001).

[66] R. Jáuregui, N. Poli, G. Roati, and G. Modugno, *Anharmonic parametric excitation in optical lattices*, Phys. Rev. A **64** (2001).

[67] T. Lauber, *A Compact and Stable Membrane-Optomechanical System*, Master's thesis, Universität Basel (2013).

[68] C. M. Wang and C. Y. Wang, *Structural Vibration : Exact Solutions for Strings, Membranes, Beams, and Plates* (CRC Press) (2014).

[69] P.-L. Yu, K. Cicak, N. S. Kampel, Y. Tsaturyan, T. P. Purdy, R. W. Simmonds, and C. A. Regal, *A phononic bandgap shield for high-Q membrane microresonators*, Appl. Phys. Lett. **104**, 023510 (2014).

[70] R. Norte, J. Moura, and S. Gröblacher, *Mechanical resonators for quantum optomechanics experiments at room temperature*, Phys. Rev. Lett. **116** (2016).

[71] B. Vogell, T. Kampschulte, M. T. Rakher, A. Faber, P. Treutlein, K. Hammerer, and P. Zoller, *Long distance coupling of a quantum mechanical oscillator to the internal states of an atomic ensemble*, New J. Phys. **17**, 043044 (2015).

[72] K. Hammerer, M. Aspelmeyer, E. S. Polzik, and P. Zoller, *Establishing Einstein-Poldosky-Rosen channels between nanomechanics and atomic ensembles*, Phys. Rev. Lett. **102** (2009).

[73] E. S. Polzik and K. Hammerer, *Trajectories without quantum uncertainties*, Ann. Phys. **527**, A15 (2014).

[74] R. J. Warburton, *Single spins in self-assembled quantum dots*, Nat. Mater. **12**, 483 (2013).

[75] N. Akopian, U. Perinetti, L. Wang, A. Rastelli, O. G. Schmidt, and V. Zwiller, *Tuning single GaAs quantum dots in resonance with a rubidium vapor*, Appl. Phys. Lett. **97**, 082103 (2010).

[76] N. Akopian, L. Wang, A. Rastelli, O. G. Schmidt, and V. Zwiller, *Hybrid semiconductor-atomic interface: slowing down single photons from a quantum dot*, Nat. Photonics **5**, 230 (2011).

UNIVERSITÄT BASEL

PHILOSOPHISCH-NATURWISSENSCHAFTLICHE FAKULTÄT

Declaration on Scientific Integrity
(including a Declaration on Plagiarism and Fraud)

~~Bachelor's~~ / Master's Thesis *(Please cross out what does not apply)*

Title of Thesis *(Please print in capital letters)*:

Dipole-Trapped Atoms at High Optical Depth for Atom-Light Quantum Interfaces

First Name, Surname *(Please print in capital letters):* Gianni Carlo Buser

Matriculation No.: 11-063-542

I hereby declare that this submission is my own work and that I have fully acknowledged the assistance received in completing this work and that it contains no material that has not been formally acknowledged.

I have mentioned all source materials used and have cited these in accordance with recognised scientific rules.

In addition to this declaration, I am submitting a separate agreement regarding the publication of or public access to this work.

☐ Yes ☒ No

Place, Date: Basel, 2.10.2016

Signature: Gianni Buser

Please enclose a completed and signed copy of this declaration in your Bachelor's or Master's thesis .

UNI
BASEL